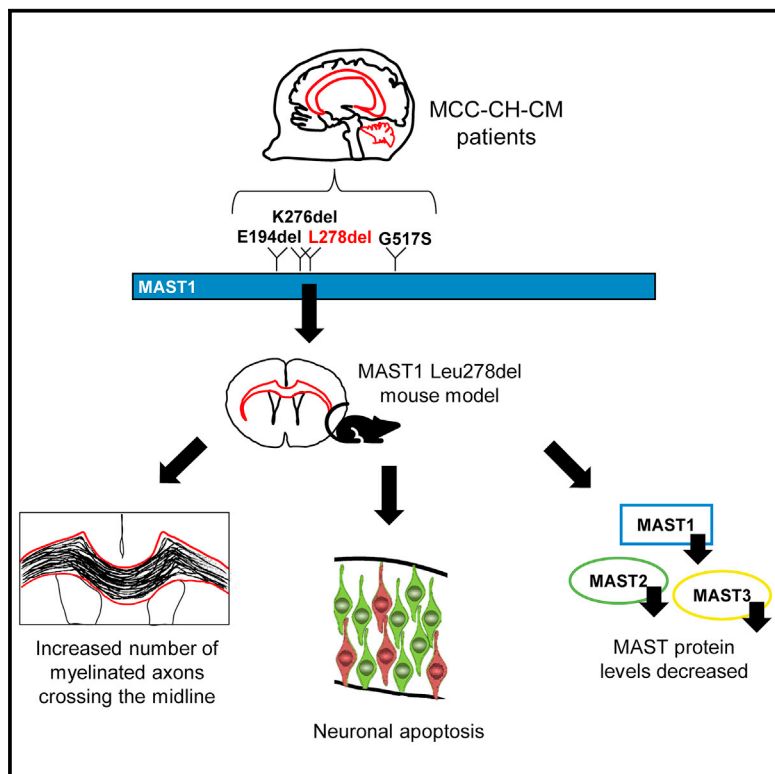


Neuron

Mutations in *MAST1* Cause Mega-Corpus-Callosum Syndrome with Cerebellar Hypoplasia and Cortical Malformations

Graphical Abstract



Authors

Ratna Tripathy, Ines Leca,
Tessa van Dijk, ..., Jamel Chelly,
Nicholas J. Cowan,
David Anthony Keays

Correspondence

keays@imp.ac.at

In Brief

Tripathy et al. show that mutations in *MAST1*, a microtubule-associated protein, cause a syndrome characterized by an enlarged corpus callosum. They attribute this thickening to an increase in the number of contralateral projections despite extensive cortical apoptosis.

Highlights

- Mast1 associates with the microtubule cytoskeleton in a MAP-dependent manner
- Mast1 is expressed in postmitotic neurons but not neuronal progenitors
- *Mast1* Leu278del mice have an enlarged corpus callosum and smaller cerebellum
- More axons cross the midline in *Mast1* Leu278del mice despite cortical apoptosis

Mutations in *MAST1* Cause Mega-Corpus-Callosum Syndrome with Cerebellar Hypoplasia and Cortical Malformations

Ratna Tripathy,¹ Ines Leca,¹ Tessa van Dijk,² Janneke Weiss,³ Bregje W. van Bon,⁴ Maria Christina Sergaki,¹ Thomas Gstrein,¹ Martin Breuss,⁵ Guoling Tian,⁶ Nadia Bahi-Buisson,⁷ Alexander R. Paciorkowski,⁸ Alistair T. Pagnamenta,⁹ Andrea Wenninger-Weinzierl,¹ Maria Fernanda Martinez-Reza,¹ Lukas Landler,¹ Stefano Lise,⁹ Jenny C. Taylor,⁹ Gaetano Terrone,¹⁰ Giuseppina Vitiello,¹⁰ Ennio Del Giudice,¹⁰ Nicola Brunetti-Pierri,^{10,12} Alessandra D'Amico,¹¹ Alexandre Reymond,¹³ Norine Voisin,¹³ Jonathan A. Bernstein,¹⁴ Ellyn Farrelly,¹⁵ Usha Kini,¹⁶ Thomas A. Leonard,¹⁷ Stéphanie Valence,¹⁸ Lydie Burglen,¹⁸ Linlea Armstrong,¹⁹ Susan M. Hiatt,²⁰ Gregory M. Cooper,²⁰ Kimberly A. Aldinger,²¹ William B. Dobyns,²¹ Ghayda Mirzaa,²¹ Tyler Mark Pierson,²² Frank Baas,² Jamel Chelly,²³ Nicholas J. Cowan,⁶ and David Anthony Keays^{1,24,*}

¹Research Institute of Molecular Pathology, Campus Vienna Biocenter 1, Vienna Biocenter (VBC), Vienna 1030, Austria

²Department of Clinical Genetics, Leiden University Medical Center, 2333 ZA Leiden, the Netherlands

³Amsterdam UMC, Vrije Universiteit Amsterdam, Clinical Genetics, De Boelelaan 1117, Amsterdam, the Netherlands

⁴Department of Human Genetics, Radboud University Medical Center, 6525 GA Nijmegen, the Netherlands

⁵Department of Neurosciences, Howard Hughes Medical Institute, University of California, San Diego, La Jolla, CA 92093, USA

⁶Department of Biochemistry & Molecular Pharmacology, NYU Langone Medical Center, New York, NY 10016, USA

⁷Université Paris Descartes, Institut Cochin Hôpital Cochin, 75014 Paris, France

⁸Department of Neurology, University of Rochester Medical Center, Rochester, NY 14642, USA

⁹NIHR Oxford Biomedical Research Centre, Oxford, UK, Wellcome Centre for Human Genetics, University of Oxford, Oxford OX3 7BN, UK

¹⁰Department of Translational Medical Sciences, Section of Pediatrics, Federico II University, 80131 Naples, Italy

¹¹Department of Advanced Medical Sciences, University of Naples Federico II, 80131 Naples, Italy

¹²Telethon Institute of Genetics and Medicine, 80078 Pozzuoli, Naples, Italy

¹³Center for Integrative Genomics, University of Lausanne, 1015 Lausanne, Switzerland

¹⁴Stanford School of Medicine, Stanford, CA 94305, USA

¹⁵Stanford Children's Health, Palo Alto, CA 94304, USA

¹⁶Department of Clinical Genetics, Oxford Regional Genetics Service, Churchill Hospital, Oxford OX3 7LJ, UK

¹⁷Center for Medical Biochemistry, Medical University of Vienna, Max F. Perutz Laboratories, Vienna Biocenter (VBC), Campus Vienna Biocenter 5, 1030 Vienna, Austria

¹⁸Centre de référence des Malformations et Maladies Congénitales du Cervelet et Département de Génétique et Embryologie Médicale, APHP, Hôpital Trousseau, 75012 Paris, France

¹⁹Provincial Medical Genetics Programme, BCWH and Department of Medical Genetics, University of British Columbia, Vancouver, BC V6H 3N1, Canada

²⁰HudsonAlpha Institute for Biotechnology, Huntsville, AL 35806, USA

²¹Seattle Children's Research Institute, Center for Integrative Brain Research, Seattle, WA 98101, USA

²²Departments of Pediatrics and Neurology & the Board of Governors Regenerative Medicine, Institute Cedars Sinai Medical Center, Los Angeles, CA 90048, USA

²³Service de Diagnostic Génétique, Hôpital Civil de Strasbourg, Hôpitaux Universitaires de Strasbourg, 67091 Strasbourg, France

²⁴Lead Contact

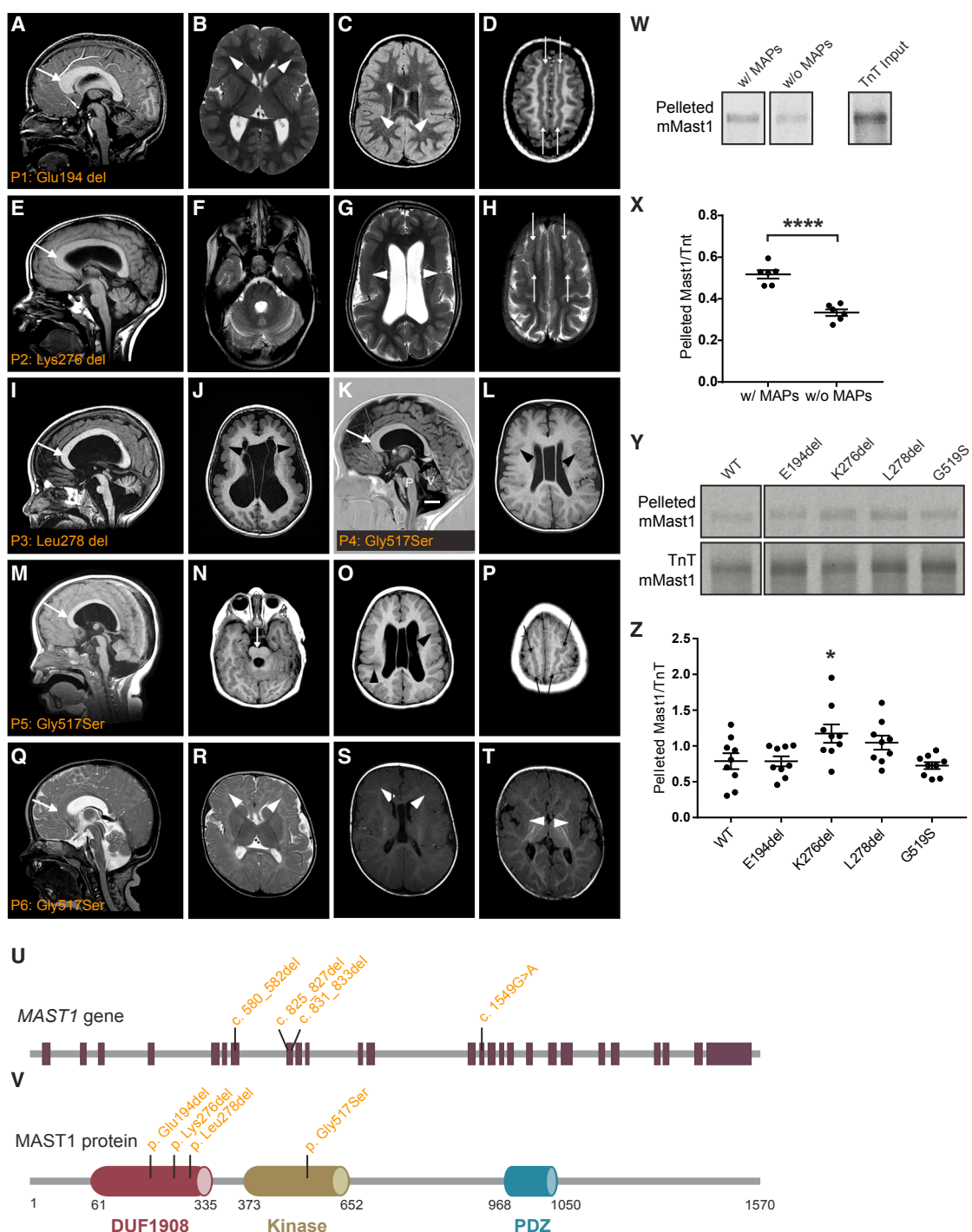
*Correspondence: keays@imp.ac.at

<https://doi.org/10.1016/j.neuron.2018.10.044>

SUMMARY

Corpus callosum malformations are associated with a broad range of neurodevelopmental diseases. We report that *de novo* mutations in *MAST1* cause mega-corpus-callosum syndrome with cerebellar hypoplasia and cortical malformations (MCC-CH-CM) in the absence of megalencephaly. We show that *MAST1* is a microtubule-associated protein that is predominantly expressed in post-mitotic neurons and is present in both dendritic and axonal compartments. We further show that *Mast1* null animals

are phenotypically normal, whereas the deletion of a single amino acid (L278del) recapitulates the distinct neurological phenotype observed in patients. In animals harboring *Mast1* microdeletions, we find that the PI3K/AKT3/mTOR pathway is unperturbed, whereas Mast2 and Mast3 levels are diminished, indicative of a dominant-negative mode of action. Finally, we report that *de novo* *MAST1* substitutions are present in patients with autism and microcephaly, raising the prospect that mutations in this gene give rise to a spectrum of neurodevelopmental diseases.



INTRODUCTION

The bilateral integration of sensory, motor, and cognitive inputs is mediated by the corpus callosum, the largest white matter tract of the brain (Paul et al., 2007). A broad array of neurodevelopmental disorders are known to be associated with malformations of this structure. For instance, corpus callosum agenesis has been reported in patients with microcephaly, lissencephaly, and polymicrogyria and has been described in patients with autism (Parrini et al., 2016). Mouse and human genetics studies have provided insight into the molecular machinery that is required for the development of this important anatomical feature (Edwards et al., 2014). It has been shown that the midline crossing of post-mitotic neurons requires transcription factors such as Satb2 (Britanova et al., 2008), cell adhesion molecules such as L1-CAM (Demyanenko et al., 1999), guidance molecules such as Netrin1 and the semaphorins (Niquille et al., 2009; Serafini et al., 1996), and cytoskeletal proteins including Map1b and the β -tubulin Tubb3 (Meixner et al., 2000; Tischfield et al., 2010). Collectively, these molecules specify the fate of neurons destined to traverse the cerebral hemispheres, guiding their leading process to the correct destination.

While thinning of the corpus callosum is relatively common, in rare instances patients present with a thickening of this myelinated structure (Edwards et al., 2014; Marsh et al., 2017). To date, this phenotype has been reported in patients with neurofibromatosis and megalencephaly-polymicrogyria-mega-corpus-callosum syndrome (DiMario et al., 1999; Göhlich-Ratmann et al., 1998). These diseases are associated with a generalized enlargement in brain size, driven by activation of the PI3K/AKT3/mTOR pathway attributable to mutations in *PIK3R2* and *NF1* (Johannessen et al., 2005; Nguyen et al., 2016; Terrone et al., 2016). As mutations in these genes do not account for all cases, it is apparent that our understanding of the molecular pathology that underlies mega-corpus-callosum syndromes is incomplete (Hengst et al., 2010). Here, we present a cohort of patients with an enlarged corpus callosum in the absence of megalencephaly, harboring mutations in the uncharacterized microtubule-associated protein (MAP) *MAST1*.

RESULTS

Identification of *MAST1* Mutations

As part of an ongoing endeavor to identify genetic variants associated with structural brain malformations, we undertook whole-exome sequencing on 7 patient-parent trios where the affected

individual presented with a striking enlargement of the corpus callosum. This led to the identification of *de novo* mutations in the gene *MAST1* (*microtubule-associated serine threonine kinase 1*) in 6 of the 7 affected individuals (Figures 1A–1T). Each of these patients presented with a hyperplastic corpus callosum (particularly over the genu and mid-body), cerebellar hypoplasia, ventricular dilation, and impaired motor and verbal performance (Table 1). Four patients presented with gyral simplification (P2 [Pierson et al., 2008], P3, P5, P6), three with dysplastic longitudinal gyri (P1, P5, P6), and one (P4) with periventricular nodules of white matter. We refer to this syndrome as mega-corpus-callosum with cerebellar hypoplasia and cortical malformations (MCC-CH-CM).

Through the Genematcher platform, four additional patients with *de novo* mutations in *MAST1* were identified who presented with either microcephaly accompanied by motor deficits (P7, P8) or autism spectrum disorder (P9, P10) (Figures S1A–S1E, Table S1) (Giliissen et al., 2014; Sobreira et al., 2015). In each case the mutation was verified by Sanger sequencing, was unreported in publicly available genome databases (e.g., dbSNP, 1000 genome, ExAC; see Table S2), and was in a highly conserved residue (Figures S1F–S1L) that was predicted to be deleterious when mutated (Table 1, Table S1, CADD score) (Kircher et al., 2014; Lek et al., 2016). We did not identify any unreported variants in our patient cohort, with the exception of a silent mutation in *TUBGCP5* (T457T) in P2 and a *de novo* mutation in NIMA related kinase 1 (NEK1) in P8 (Table 1, Table S1). It should be noted that mutations in NEK1 have been previously associated with amyotrophic lateral sclerosis, ciliary dysfunction, and skeletal diseases; however, patient P8 did not present with symptoms consistent with these disorders (Kenna et al., 2016; Thiel et al., 2011). Three of the MCC-CH-CM-associated variants in *MAST1* were single amino acid deletions positioned in the hydrophobic core of a four-helix bundle in the domain of unknown function DUF1908 (P1, p.Glu194del; P2, p.Lys276del; P3, p.Leu278del) (Figure S1M), while the remainder (P4–P6, p.Gly517Ser) harbored a recurrent missense mutation in the kinase domain of the protein (Figures 1U and 1V). These microdeletions were not found in control individuals in the ExAC genome browser; however, a single microdeletion between the kinase and PDZ domains (Glu697del) has been reported (Table S2).

MAST1 Is a Microtubule-Associated Protein

Little is known of the function of the MAST family of proteins (MAST1–4). MAST2 was initially cloned from testes and was

(U) Schematic representation of the *MAST1* genomic locus shows the position of the mutations identified in patients P1–P6.

(V) The *MAST1* protein consists of a domain of unknown function (DUF1908, shown in red), a kinase domain (shown in yellow), and a PDZ domain (shown in blue). The amino acid boundaries of each of the domains are shown.

(W–Z) Autoradiograph showing the results of the microtubule binding assay with Mast1. Murine Mast1 was radiolabeled (35 S) by *in vitro* transcription and translation (TnT) in rabbit reticulocyte lysate, before incubation with a porcine microtubule extract in the presence or absence of microtubule-associated proteins (MAPs) (W and X). Following microtubule polymerization in the presence of Taxol, pelleted microtubules were analyzed by polyacrylamide gel electrophoresis (PAGE), and the ratio of pelleted radiolabeled-mMast1 to TnT input was determined. This experiment revealed a decrease of binding of Mast1 to microtubules in the absence of MAPs (X; n = 6 technical replicates; two-tailed unpaired t test; t7 = 7.134, p < 0.0001). Patient mutations were introduced into mMast1, radiolabeled by *in vitro* TnT, and microtubule binding was assessed (Y and Z). The ratio of microtubule-bound Mast1 (in the pelleted fraction) to TnT input was determined. Comparison of pelleted wild-type Mast1 to the K276del mutation shows a significant alteration in microtubule binding and a similar trend for the L278del (Z; n = 6–9 repeated experiments; one-way ANOVA with Dunnett's multiple comparison; WT versus K276del p < 0.05).

*p < 0.05; **p < 0.01; ***p < 0.001; ****p < 0.0001. Error bars show mean \pm SEM.

Table 1. Clinical Summary of Patients with MCC-CH-CM

Patient	P1	P2	P3	P4	P5	P6
Mutation (chr19)	19:12958677delGAG	chr19:12962798delGAA	chr19:12962804delGTT	19:12975903G>A	19:12975903G>A	19:12975903G>A
Mutation (NM_014975.2)	Glu194del c.580_582del	Lys276del c.825_827del	Leu278del c.831_833del	Gly517Ser c.1549G>A	Gly517Ser, c.1549G>A	Gly517Ser, c.1549G>A
CADD v1.3	16,71	17,35	21,4	27,9	27,9	27,9
Inheritance	<i>de novo</i>	<i>de novo</i>	<i>de novo</i>	<i>de novo</i>	<i>de novo</i>	<i>de novo</i>
Ethnicity	Caucasian	Caucasian	Caucasian	Moroccan	Caucasian	Caucasian
Geographic ancestry	Italian	Hungarian	French	Moroccan	Unknown	French
Sex	Male	Male	Female	Female	Female	Female
Age at last evaluation	9 years	11.5 years	6 years	6 years	10 years	1.5 year
OFC ^a at birth	Unknown	36.5 cm (50 th –75 th percentile)	Unknown	Unknown	Unknown	35 cm (50 th percentile)
OFC ^a	52 cm	53 cm (25 th –50 th percentile)	51 cm	52 cm (+0.6 SD)	49.2 cm at 2 years, 9 months (50 th percentile)	46.5 cm at 18 months
Cortical dysgenesis	Dysplastic longitudinal gyri; subependymal heterotopias	Extensive undersulcated gyral pattern over frontal, temporal, and perisylvian regions; dysplastic longitudinal gyri	Tubulinopathy-like dysgyria with mildly thick cortex and diffuse very shallow sulci	Periventricular lesions	Diffuse subtle dysgyria; radial/shallow sulci with some deep infolds; dysplastic longitudinal gyri	Subtle frontal dysgyria; dysplastic longitudinal gyri
Basal ganglia	Normal	Poorly developed	Normal	Normal	Normal	Normal
Cerebellum	Vermis hypoplasia (++) ; counterclockwise rotation of cerebellar vermis	Mild diffuse cerebellar hypoplasia (+) with prominent sulci	Hypoplasia (++)	Hypoplasia (++)	Vermis hypoplasia (++) and mild hemispheric hypoplasia	Vermis hypoplasia (++) and mild hemispheric hypoplasia
Brainstem	Hypoplasia (++)	Small pons (+)	Hypoplasia (++)	Pontine hypoplasia (++)	Severe brainstem hypoplasia with a very small pons (++), thin midline cleft, long and mildly enlarged medulla	Severe brainstem hypoplasia (++) , small pons with relative sparing of its bulding
Corpus callosum	Hyperplasia, mostly over genu and anterior body (++)	Very thick and dysplastic corpus callosum (mega corpus callosum) (++)	Hyperplastic (++)	Hyperplasia, mostly over genu and anterior body (+)	Thick corpus callosum (+)	Thick corpus callosum (+)
Ventricular dilation	Enlarged 4 th ventricle (+)	Enlarged 3 rd ventricle (++)	Enlarged 3 rd ventricle (++)	Enlarged 4 th ventricle (++)	Enlarged 3 rd and 4 th ventricles (++)	(+)
Cognitive abilities	Moderate cognitive impairment	Intellectual disability	Severe encephalopathy	Severe intellectual disability	Global developmental delay	Global developmental delay
Verbal abilities	Poor	Non-verbal	Non-verbal	Non-verbal	Non-verbal	Only some sounds (vowels)

(Continued on next page)

Patient	P1	P2	P3	P4	P5	P6
Motor abilities	Clumsy stumbling gait, generalized hypotonia	Generalized hypotonia, mild truncal ataxia	Severe hypotonia	Able to stand with support, hyperreflexia	Can sit up by herself with assistance from her arms; able to roll	Hypotonic, sitting; with cyphosis, and only with support on arms; able to roll
Other	Short stature, paroxysmal EEG abnormalities (spike-wave complexes) with no clinical seizures	Infantile-onset epilepsy, oculomotor apraxia	None	Short stature, strabismus	Seizures (onset 6 years), history of aspiration	Head thrusts suggestive of oculomotor abnormality
Other <i>de novo</i> or novel variants	None	Inherited a novel silent mutation in TUBGCP5: chr15 (22851109) C>T (T457T)	None	None	None	None
^a OFC, occipitofrontal circumference						

^aOFC, occipitofrontal circumference

shown to function as a kinase and interact with microtubules via other MAPs (Walden and Cowan, 1993). To ascertain whether *MAST1* associates with the microtubule cytoskeleton, we performed an *in vitro* transcription and translation (TnT) reaction employing rabbit reticulocyte lysate with radiolabeled murine (m) Mast1 (which shares 94% sequence identity with human *MAST1*). The reaction products were then assayed for their ability to bind to microtubules in the absence or presence of MAPs. We found that mMast1 associates with Taxol-stabilized microtubules in a MAP-dependent manner (Figures 1W and 1X; n = 6; p < 0.0001). Next, we asked whether the *MAST1* mutations found in our patient cohort influence microtubule binding. We introduced each mutation into our pcDNA 3.1 vector, labeled Mast1 with ³⁵S-methionine, and repeated the aforementioned microtubule binding assay. While translation efficiency was similar for all variants, we found that the K276 deletion significantly enhanced Mast1 binding to microtubules (Figures 1Y and 1Z; n = 9; WT versus K276del p < 0.05). Taken together, these data show that Mast1 binds to microtubules in a MAP-dependent manner and that mutations can perturb this interaction.

***MAST1* Is Expressed in Post-mitotic Neurons**

To gain insight into the role of *MAST1* in neurodevelopment, we analyzed its expression in the human and mouse brain during early developmental stages (Figures 2A and 2B). To this end we extracted mRNA from the developing murine brain (E10.5, E12.5, E14.5, E16.5, E18.5, P0, and P6), generated cDNA, and performed qPCR analysis. We observed that Mast1 expression begins at E12.5, peaks at E16.5, and decreases postnatally (Figure 2B). Consistent with this result, qPCR analysis of human fetal brain cDNA showed moderate expression of *MAST1* at gestation weeks 13 and 22 (Figure 2A). To determine which cells express Mast1, we performed immunohistochemistry on the murine cortex at E12.5, E14.5, E16.5, and P0 (n = 3). We used a commercially available Mast1 antibody, having validated its specificity employing a Mast1 knockout (KO) animal (Figures S3B–S3D). We observed staining in the developing cortical plate and intermediate zone at these time points (Figures 2C–2F). Further analysis at E14.5 and E16.5 showed that Mast1 is located in the cytoplasm in Tuj-positive post-mitotic neurons but is largely absent from Sox2-positive progenitors and Tbr2-positive intermediate progenitors (Figures 2S–2AP) (n = 3). This expression pattern is mirrored in human cerebral organoids that were cultured for 64 days, where we again observed co-localization with post-mitotic markers (Figures S2A–S2F) (n = 10 organoids) (Lancaster et al., 2013). Immunostaining on P0 mouse brain sections showed that Mast1 is present in Tuj-positive corpus callosal fibers that cross the midline (n = 3) (Figures S2G–S2L). To gain further insight into the subcellular localization of Mast1, we cultured primary P0 cortical neurons and P7 cerebellar granule neurons and performed immunostaining. We again validated the specificity of our Mast1 antibody for cell culture experiments employing a *Mast1* KO animal (Figure S2S–T). We performed double staining with antisera specific for the axonal marker Tau or the dendritic marker Map2 (Kosik and Finch, 1987). We observed Mast1 staining throughout the soma, as well as in dendritic and axonal compartments in cortical neurons (Figures 2G–2R, n = 5) and in cerebellar granule neurons

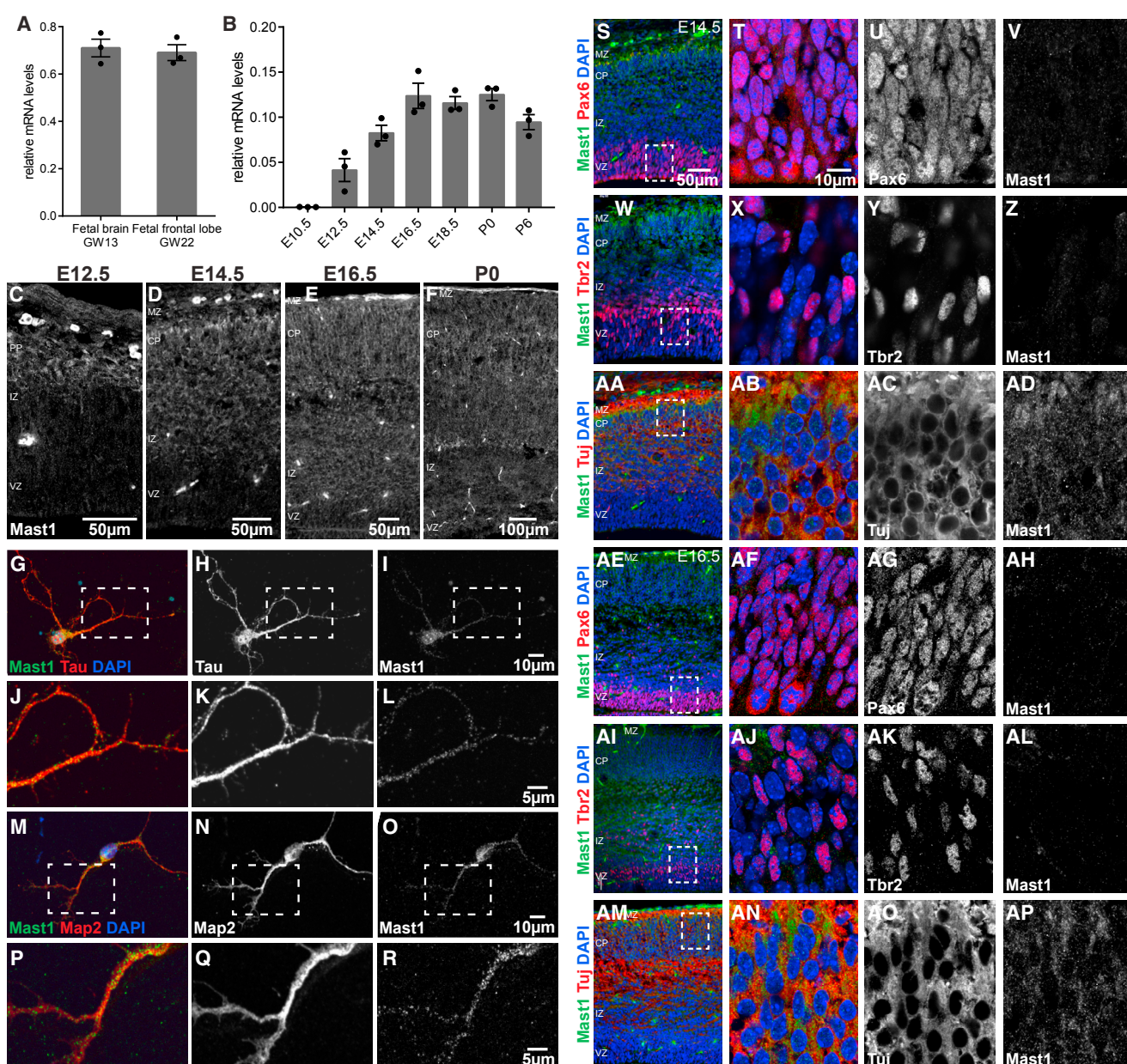


Figure 2. Mast1 Expression in Human and Mouse Embryonic Brain

(A) qPCR analysis reveals that *MAST1* mRNA is expressed in the human developing fetal brain at gestational week (GW) 13 and the fetal frontal lobe at GW22. (B) qPCR analysis performed on mouse brain cDNA libraries from E10.5 to P6 show that Mast1 expression peaks at E16.5 in mice ($n = 3$ animals per time point). (C–F) Immunohistochemistry employing a validated Mast1 antibody (see also Figures S3B–S3D) indicates staining in the post-mitotic cortical plate and intermediate zone from E12.5 to P0 in mice.

(G–R) Maximum-projection images of cultured P0 cortical neurons at 5-DIV staining with the axonal marker Tau (G–L) and the dendritic marker Map2 (M–R) show that Mast1 (I, L, O, and R) is present in both axonal and dendritic compartments. Dashed boxes in (G)–(I) and (M)–(O) are expanded in (J)–(L) and (P)–(R), respectively.

(S–AP) Immunohistochemistry employing the progenitor marker Pax6 (S–U and AE–AG), intermediate progenitor marker Tbr2 (W–Y and AI–AK), and post-mitotic marker Tuj (AA–AC and AM–AO) on E14.5 (S–AD) and E16.5 (AE–AP) murine sections reveals that Mast1 expression is restricted to post-mitotic neurons at these time points (PP, preplate; CP, cortical plate; MZ, marginal zone; IZ, intermediate zone; VZ, ventricular zone).

Error bars show mean \pm SEM.

(Figures S2M–S2R, $n = 3$). This staining had a punctate appearance, suggesting that Mast1 may associate with vesicular structures that are trafficked along the microtubule cytoskeleton.

qPCR analysis of Mast1 expression in the adult mouse showed that its expression persists in all brain regions (albeit at much lower levels) and that it is present in the testes, liver, and spleen

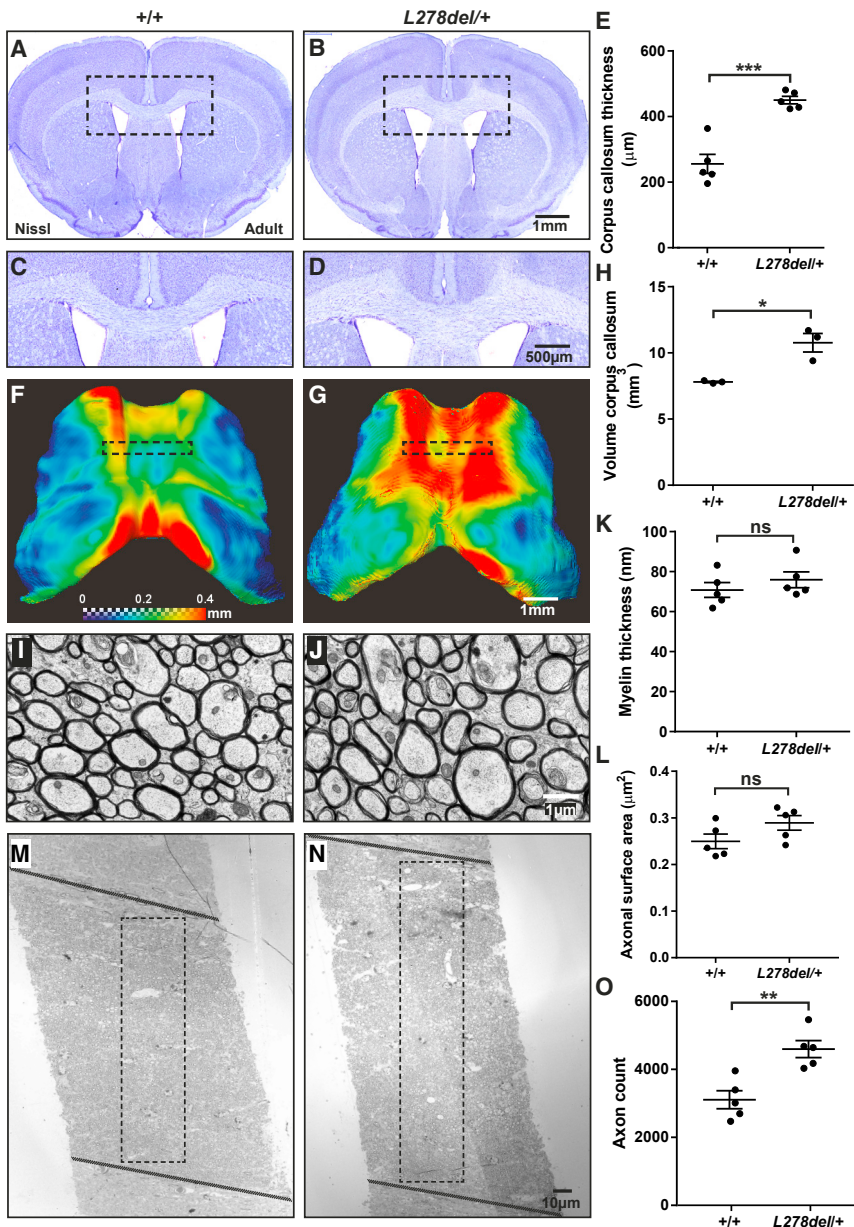


Figure 3. *L278del* Mice Have an Enlarged Corpus Callosum Associated with an Increase in the Number of Callosal Axons

(A–D) Nissl-stained sections of 8-week-old adult brains highlighting the thicker corpus callosum in *L278del/+* animals compared to wild-type littermates (black boxes in A and B are expanded in C and D).

(E) Quantification of the thickness at the septum reveals a significantly thicker corpus callosum in *L278del/+* animals ($n = 5$ animals per genotype; unpaired t test; $+/+$ versus *L278del/+*; $t_8 = 6.217$, $p < 0.001$).

(F and G) MRI reconstructions of the corpus callosum in wild-type controls (F) and *L278del/+* mice (G). The heatmap reflects the thickness of the corpus callosum (blue, thinner region; red, thicker region). Note that in *L278del/+* animals the genu and midbody region are most affected.

(H) MRI volumetric quantification of the corpus callosum shows that this structure is significantly larger in *L278del/+* animals compared to wild-type littermates ($n = 3$ animals per genotype; two-tailed unpaired t test; $+/+$ versus *L278del/+*; $t_4 = 4.233$, $p < 0.05$).

(I and J) Electron microscopy images showing cross-sections of the corpus callosum at the midbody (region depicted with boxes in F and G). Myelinated axons can be clearly visualized.

(K) Quantification of myelin thickness reveals no significant difference between *L278del/+* animals and wild-type littermates ($n = 5$ animals per genotype, >500 myelinated axons per animal; two-tailed unpaired t test; $t_8 = 1.001$, $p > 0.1$).

(L) Quantification of axonal caliber reveals no significant difference between *L278del/+* animals and wild-type littermates ($n = 5$ animals per genotype, $>1,500$ myelinated axons per animal; $+/+$ versus *L278del/+*; two-tailed unpaired t test; $t_8 = 1.786$, $p > 0.1$; see also Figure S3N).

(M and N) Assessment of the total number of myelinated axons within a 30-μm-wide box extending along the ventro-dorsal axis of the corpus callosum.

(O) Quantification reveals a significant increase in axonal count in the *L278del/+* animals in comparison to wild-type littermates ($n = 5$ animals per genotype, 3 images analyzed per animal; two-tailed unpaired t test; $t_8 = 4.095$, $p < 0.01$).

* $p < 0.05$; ** $p < 0.01$; *** $p < 0.001$; **** $p < 0.0001$. Error bars show mean ± SEM.

at very low levels ($n = 3$) (Figure S2U). These results are consistent with expression data that are available through online databases (e.g., Allen Brain Atlas, GTEx) (GTEx Consortium, 2013; Morris et al., 2010). Taken together, these data show that *Mast1* is predominantly expressed in post-mitotic neurons in the developing nervous system.

An Enlarged Corpus Callosum in a *L278Del Mast1* Mouse Model

To investigate the effect of *Mast1* mutations *in vivo*, we exploited the power of the CRISPR-Cas9 genome editing system to generate a *Mast1* KO mouse and a *Mast1 L278del* (*L278del*) mouse employing guide RNAs targeted to exon 8 (Figure S3A)

(Wang et al., 2013). We decided to recapitulate the mutation identified in patient P3 because of the striking callosal, cortical, and cerebellar phenotypes. As homozygous *L278del/del* animals die shortly after birth, we focused our initial analysis on homozygous *Mast1* KO and heterozygous *L278del/+* mice, which are viable. We analyzed the thickness of the genu of the corpus callosum on rostral Nissl-stained coronal sections (bregma 0.86 mm). While *Mast1* KO animals were indistinguishable from wild-type littermate controls (Figures S3E–S3G; $n = 5$; $+/+$ versus *KO/KO*; $p > 0.5$), *L278del/+* animals presented with a significantly thicker corpus callosum in comparison to wild-type littermate controls (Figures 3A–3E; $n = 5$; $+/+$ versus *L278del/+*; $p < 0.001$). High-resolution volumetric magnetic

resonance imaging (MRI) analysis confirmed an increased corpus callosum volume in *L278del/+* animals (Figure 3H; n = 3; +/+ versus *L278del/+*; p < 0.05) and revealed that the thickening was most prominent in the rostral regions encompassing the genu and the mid-body (Figures 3F and 3G). The enlarged corpus callosum was also present in *L278del* mice aged 10 days (Figures S3K–S3M; n = 5; +/+ versus *L278del/+*; p < 0.05). While off-target mutations in Cas9-modified mice are rare (Iyer et al., 2015), we confirmed that this phenotype was not due to a linked mutation by undertaking whole-exome sequencing for our *L278del/+* mouse line. We identified no other non-synonymous mutations on chromosome 8 in this line (Table S3). Moreover, we generated a second independent *L278del* mouse line and once again observed an enlarged corpus callosum (Figures S3H–S3J; +/+ versus *L278del/+_Line#7*; n = 3; p < 0.01).

We then asked whether the increase in the thickness of the corpus callosum of the *L278del/+* mice was due to an increase in the thickness of myelinated axons. In light of our MRI studies, we focused our analysis on the midbody of the corpus callosum, where we observe the most pronounced phenotype in *L278del/+* mutants (bregma –0.10). The corpus callosum of adult animals was microdissected, samples were stained to enable clear visualization of myelinated neurons crossing the midline, and images captured at high resolution (8,900 \times) with transmission electron microscopy (Figures 3I and 3J) (Sturrock, 1980; West et al., 2015). We observed no significant difference in either myelin thickness (Figure 3K; n = 5; n > 500 axons per animal; +/+ versus *L278del/+*; p > 0.1) or axonal caliber (Figure 3L; n = 5; n > 1500 axons per animal; +/+ versus *L278del/+*; p > 0.1) when comparing littermate controls with *L278del/+* animals. An analysis of the distribution of axon calibers in *L278del/+* animals again revealed no significant difference in comparison to littermate controls (n = 5; +/+ versus *L278del/+*; p > 0.1 for all bins) (Figure S3U). Reflecting this, an assessment of the G-ratio (axonal diameter/total fiber diameter), revealed no significant difference between genotypes (n = 5, n > 300 fibers animal, +/+ versus *L278del/+*; p > 0.1) (Figure S3N) (Guy et al., 1989).

Given these results, we asked whether more myelinated axons might cross the midline in *L278del/+* animals. To assess this, TEM images were acquired at a magnification of 710 \times along the dorso-ventral axis of the corpus callosum. These images (10–12 per animal) were tiled, resulting in a single image that encompassed the entire cross-section of the corpus callosum. A box 30 μ m wide was overlaid onto the structure, and the total number of myelinated axons was counted manually (Figures 3M and 3N). Statistical analysis revealed a significant increase in the number of myelinated axons within that box in *L278del/+* animals in comparison to littermate controls (Figure 3O; n = 5 animals per genotype, n = 3 images per animal, +/+ versus *L278del/+*; p < 0.01). Finally, we counted the number of Olig2-positive oligodendrocytes and GFAP-positive astrocytes in a box of fixed width that was overlaid onto coronal sections of the corpus callosum (Figures S3O–S3R). This revealed that in *L278del/+* animals there are more oligodendrocytes and astrocytes in comparison to wild-type controls (n = 5; +/+ versus *L278del/+*; Olig2, p < 0.05; GFAP, p < 0.05) (Figures S3S and S3V). There was, however, no significant difference in the density of these

cell types when comparing genotypes (n = 5; +/+ versus *L278del/+*; Olig2, p > 0.5; GFAP, p > 0.05) (Figures S3T and S3W). Taken together, these data show that our *L278del/+* mouse model recapitulates the enlarged corpus callosum observed in affected patients, which we attribute to an increase in the number of myelinated axons crossing the midline.

Cortical and Cerebellar Hypoplasia in the *L278del Mast1* Mouse Model

We extended our analysis of the *L278del* and *KO* mouse lines to the cortex and cerebellum, which are consistently affected in our *MAST1* patient cohort. MRI volumetric analysis of adult animals revealed an overall reduction in cortical volume in *L278del* heterozygotes (Figures 4A–4C; n = 3; +/+ versus *L278del/+*; p < 0.05). We confirmed this finding by undertaking Nissl and NeuN staining, where we observed a significant reduction in cortical thickness in *L278del* animals that was most pronounced in caudal regions (bregma –1.82 mm; Nissl [Figures 4D–4F]; n = 5, +/+ versus *L278del/+*, p < 0.001; NeuN [Figures S4A–S4D]; n = 5; +/+ versus *L278del/+*; p < 0.0001). We did observe a reduction in cortical thickness in the rostral motor cortex in *L278del* heterozygotes (bregma 0.86 mm); however, this was not statistically significant (Figures S4E–S4G, n = 5; +/+ versus *L278del/+*; p > 0.1). We assessed the thickness of the cortical layers in the affected caudal regions in *L278del* heterozygotes and littermate controls. We observed a significant reduction in the thickness of layer 5, marked by the transcription factor Er81 (Figures 4J–4L; n = 5; +/+ versus *L278del/+*; p < 0.01). We did not observe a significant difference in the thickness of Foxp2-positive layer VI neurons (Figures S4H–S4K; n = 5; +/+ versus *L278del/+*; p > 0.1) (Ferland et al., 2003) or Cux1-positive granule cells (Figures 4G–4I; n = 5; +/+ versus *L278del/+*; p > 0.5) (Cubelos et al., 2015). Analysis of the caudal cortex at P10 by Nissl staining again revealed that it was thinner in *L278del/+* mutants (Figure S4U; n = 5; +/+ versus *L278del/+*; p < 0.01). Consistent with our previous findings, adult *Mast1* KO animals appeared to be phenotypically normal, without morphological or layering defects in the adult *KO* cortex (Figures S4A–S4D and S4H–S4T).

MRI volumetric analysis of the cerebellum revealed a severe reduction in *L278del* heterozygotes (Figures 5A–5C; n = 3; +/+ versus *L278del/+*; p < 0.001). Nissl staining as well as NeuN and calbindin immunohistochemistry showed that the foliation and lamination of the cerebellum in *L278del* heterozygotes was comparable to wild types; however, the granule and the molecular cell layer appeared thinner in mutants (Figures 5D–5I). We calculated the density of granule cells as well as the linear density of Purkinje cells, allowing us to estimate the total number of these cell types in midsagittal sections. While the density of both cell types was similar in *L278del* mutants in comparison to littermate controls (Figures S5A and S5B), we observed a significant reduction in the total number of granule cells per section (Figure 5J; n = 5; +/+ versus *L278del/+*; p < 0.05). We also observed a reduction in the total number of Purkinje cells per section, but this reduction was not statistically significant (Figure 5K; n = 5; +/+ versus *L278del/+*; p > 0.5). Volumetric analysis of the colliculi, putamen, thalamus, and olfactory bulbs revealed no significant difference between wild-type littermates and

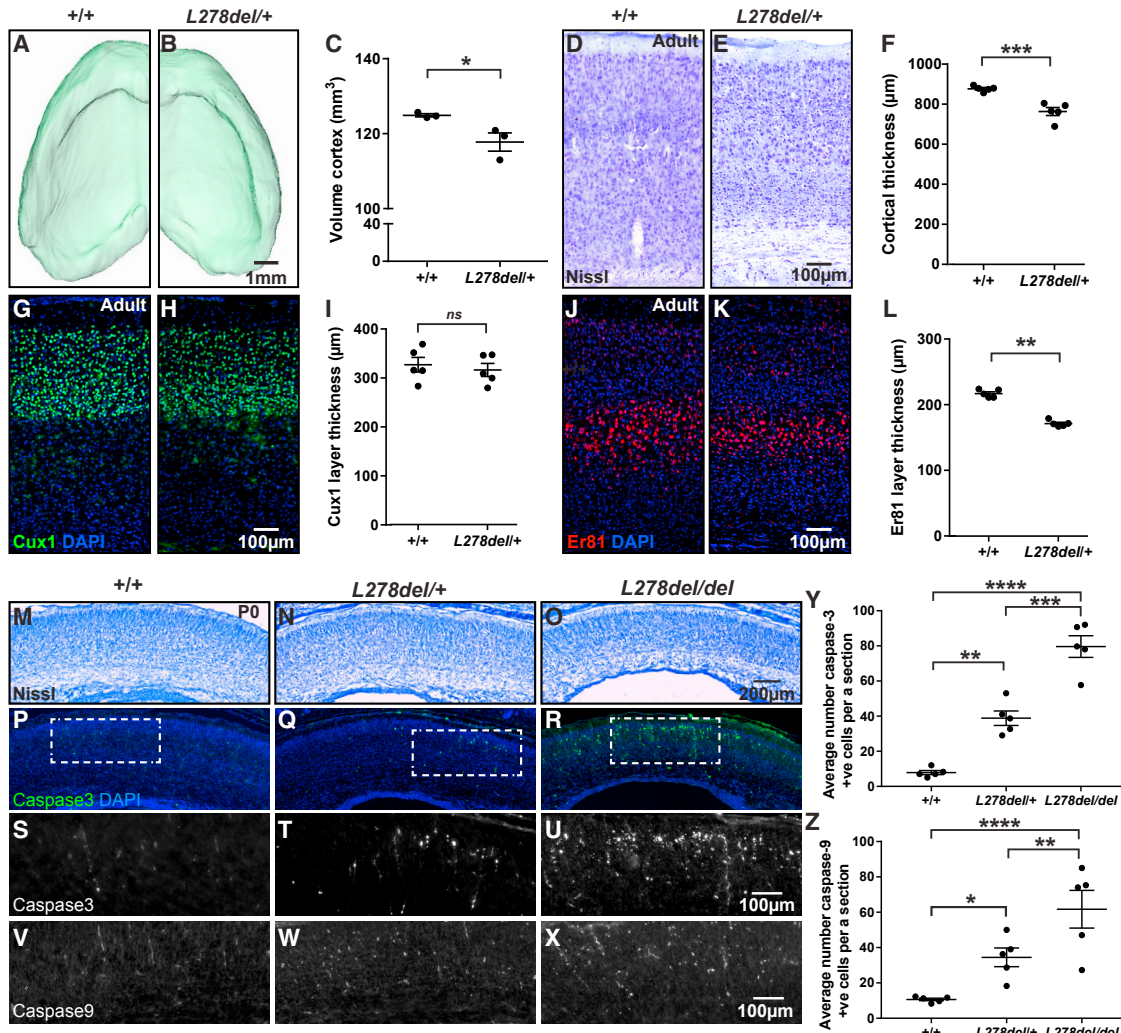


Figure 4. L278del Mice Have a Reduction in Cortical Volume Associated with an Increase in Neuronal Apoptosis

(A and B) MRI reconstructions of the cortex in adult animals reveal a reduction in cortical volume in *L278del/+* mice in comparison to littermate controls.

(C) Quantification of the MRI cortical volume (n = 3 animals per genotype; two-tailed unpaired t test; +/+ versus *L278del/+*; t4 = 2.902, p < 0.05).

(D and E) Nissl-stained sections of the adult somatosensory cortex reveal a reduction in cortical thickness in *L278del/+* adult mice in comparison to littermate controls.

(F) Quantification of caudal cortical thickness (n = 5 animals per genotype; two-tailed unpaired t test; +/+ versus *L278del/+*; t8 = 5.417, p < 0.001).

(G–L) Labeling of Cux1-positive layer II–III (G and H) and Er81-positive layer 5 neurons in wild-type and *L278del/+* adult mice (J and K). Quantification (I) reveals no significant difference in Cux1 layer thickness when comparing genotypes but a significant reduction in the size of the Er81-positive layer (L) (n = 5 animals per genotype; two-way repeated-measures ANOVA with a Bonferroni test for multiple comparisons; +/+ versus *L278del/+*; Cux1 layer p > 0.1; Er81 layer p < 0.01). (M–X) Representative Nissl-stained (M–O), activated caspase-3-stained (P–U), and activated caspase-9-stained (V–X) P0 cortical sections of littermate controls (M, P, S, and V), *L278del/+* (N, Q, T, and W), and *L278del/del* (O, R, U, and X) animals. The white boxes in (P), (Q), and (R) are expanded in (S), (T), (U). The number of caspase-3-positive and caspase-9-positive cells in the cortex of P0 animals was counted and averaged (3 sections per animal). There is a dose-dependent increase in apoptotic cells in *L278del/+* and *L278del/del* animals in comparison to littermate controls (see also Figure S4V).

(Y and Z) Quantitation of caspase-3 (Y) and caspase-9 (Z) staining (n = 5 animals per genotype; n = 3 sections per animal; two-way repeated-measures ANOVA with a Bonferroni test for multiple comparison. Caspase-3: +/+ versus *L278del/+* p < 0.01; +/+ versus *L278del/del* p < 0.0001; *L278del/+* versus *L278del/del* p < 0.001. Caspase-9: +/+ versus *L278del/+* p < 0.05; +/+ versus *L278del/del* p < 0.0001; *L278del/+* versus *L278del/del* p < 0.01).

*p < 0.05; **p < 0.01; ***p < 0.001; ****p < 0.0001. Error bars show mean ± the SEM.

L278del heterozygotes (Figure S5C; n = 3; +/+ versus *L278del/+*; p > 0.5 for all regions). There was a reduction in the volume of the hippocampus in *L278del* heterozygotes, but this difference was not statistically significant (Figure S5C; n = 3; +/+ versus *L278del/+*; p = 0.34).

Neuronal Apoptosis in the *L278del* Mast1 Mouse Model

To determine if the smaller cortex and cerebellum in our *L278del* mutant mice is a result of neuronal cell death during development, we performed an activated caspase-3 staining. We detected a dose-dependent increase in the number of apoptotic

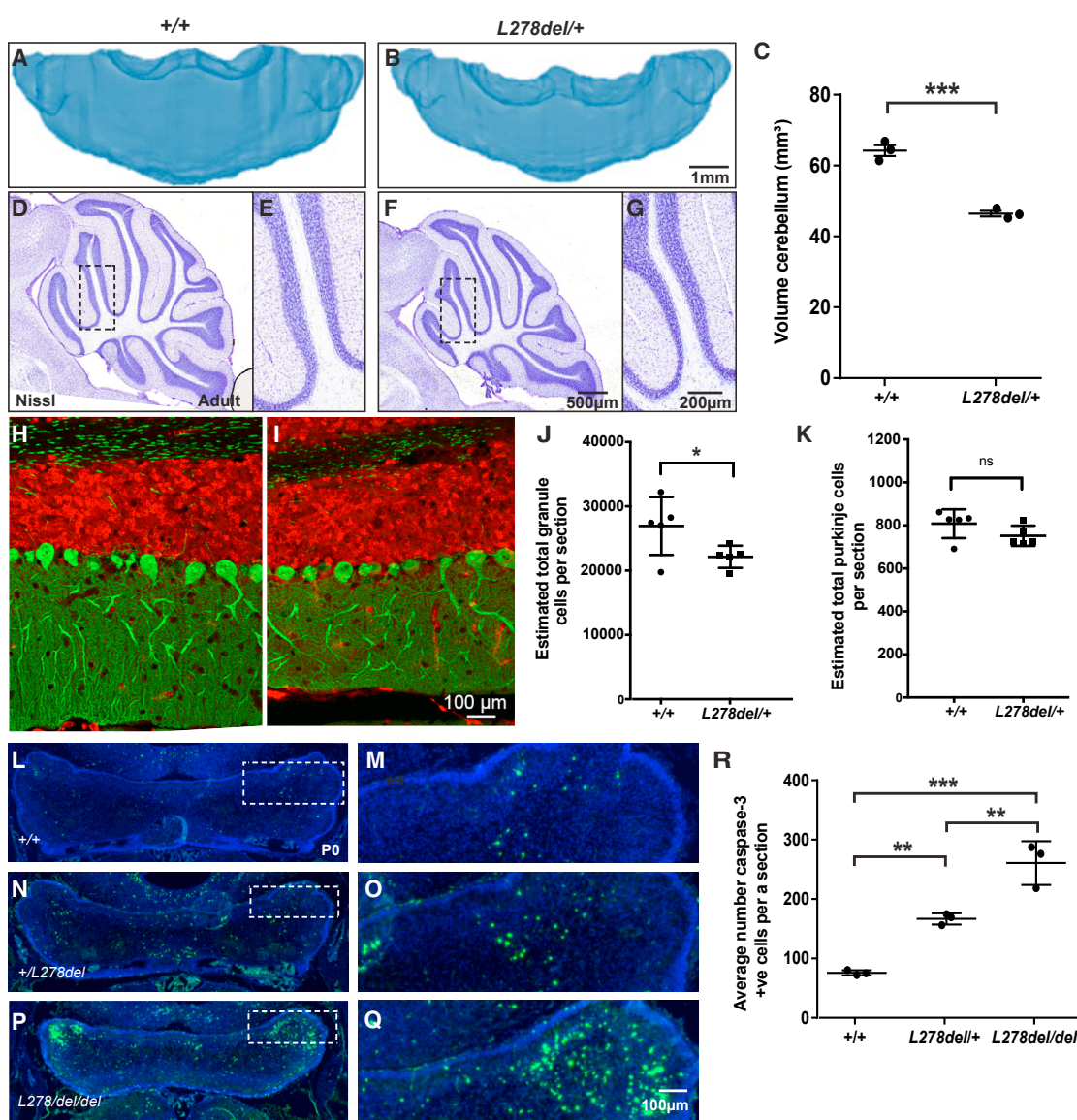


Figure 5. L278del/+ Mice Have a Hypoplastic Cerebellum

(A and B) MRI reconstructions of the cerebellum from wild-type littermates (A) and L278del/+ (B) adult animals.

(C) Quantification reveals a significant reduction in cerebellar volume (mm³) in L278del/+ animals (n = 3 animals per genotype; two-tailed unpaired t test; +/+ versus L278del/+; t₄ = 10.16, p < 0.001).

(D–G) Nissl-stained sagittal sections of 8-week-old cerebellum confirm the reduction in cerebellar size and indicate that lamination within the cerebellum is normal in L278del/+ animals.

(H and I) Immunostaining employing the neuronal marker NeuN (shown in red) and the Purkinje cell marker Calbindin (shown in green) revealed a reduction in the thickness of the granule cell layer and molecular layer in L278del/+ animals.

(J and K) Estimates of the total number of granule cells (J) and Purkinje cells (K) per a midsagittal section in L278del/+ animals and littermate controls (n = 5 animals per genotype; two-way ANOVA with a Bonferroni correction; +/+ versus L278del/+; granule cell counts: p < 0.05; Purkinje cell counts: p > 0.5; see also Figures S5A and S5B).

(L–Q) Immunohistochemistry employing sera for activated caspase-3 reveals an increase in apoptosis in the L278del/+ and L278del/del animals in the developing cerebellum at P0. The white boxes in (L), (N), and (P) are expanded in (M), (O), and (Q), respectively.

(R) Quantification of caspase-3 staining (n = 3 animals per genotype; one-way ANOVA with Tukey's multiple-comparisons test; +/+ versus L278del/+ p < 0.01; +/+ versus L278del/del p < 0.001; L278del/+ versus L278del/del p < 0.01).

*p < 0.05; **p < 0.01; ***p < 0.001; ****p < 0.0001. Error bars show mean ± the SEM.

cells in the P0 cortex of wild-type versus heterozygous and homozygous *L278del* mice (Figures 4P–4U, 4Y, and S4 AB; n = 5; +/+ versus *L287del/+* p < 0.01; +/+ versus *L278del/del* p < 0.0001; *L278del/+* versus *L278del/del* p < 0.001). Consistent with our anatomical analysis of adult animals, we found that apoptosis was more severe in the caudal regions of the P0 cortex in the *L278del/+* and *L278del/del* animals (Figure S4V; n = 5; rostral versus caudal: *L278del/+* p < 0.001; *L278del/L278del* p < 0.0001). At P10 and in 8-week-old adult mice, apoptosis in *L278del/+* mice was comparable to wild-type controls (Figures S4W–S4Z; n = 5; +/+ versus *L278del/+*; P10, p > 0.1; Adult: p > 0.1). An analysis of activated caspase-3 staining in the P0 cerebellum revealed a large increase in *L278del/+* and *L278del/del* animals in comparison to wild-types (Figures 5L–5R; n = 3; +/+ versus *L278del/+* p < 0.01; +/+ versus *L278del/del* p < 0.001; *L278del/+* versus *L278del/del* p < 0.01). To ascertain whether this cell death is associated with intrinsic suicide pathways, we stained P0 cortical sections with sera that target activated caspase-9, an upstream regulator of caspase-3 that is associated with mitochondrial mediated apoptosis (Hyman and Yuan, 2012). We observed a dose-dependent increase in the number of activated caspase-9-positive cells in the cortex of heterozygous and homozygous *L278del* mice (Figures 4V–4X and 4Z; n = 5; +/+ versus *L278del/+* p < 0.05; +/+ versus *L278del/del* p < 0.0001; *L278del/+* versus *L278del/del* p < 0.01). Intriguingly, this was not associated with the upregulation of the tumor suppressor p53 (Figures S4AA–S4AF), which has been associated with a range of stressful cellular events including DNA damage, defects in cell cycle progression, as well as oxidative and nutritional stress (Szybińska and Leśniak, 2017). Taken together, these data show that the *L278del* mutation results in a hypoplastic cortex and cerebellum, a phenotype that is associated with neuronal apoptosis mediated by activated caspases 3 and 9, but not p53 upregulation.

The L278 Microdeletion Alters Mast1/2/3 Protein Levels but Not the PI3K/AKT3/mTOR Pathway

Next, we exploited these mouse models to investigate the underlying molecular impairment associated with *MAST1* mutations. Western blot analysis of P0 brain lysates showed a complete absence of Mast1 protein in KO animals (n = 6), with an unexpected dose-dependent reduction in Mast1 levels in the *L278del* line (Figure 6A–D; n = 4, Mast1: +/+ versus *L278del/+* p < 0.0001; +/+ versus *L278del/Ldel* p < 0.0001). This absence of protein in the *Mast1* KO animals correlates with a dramatic reduction in mRNA levels, but this is not the case in *L278del* mice, where *Mast1* transcript levels are statistically similar in +/+, *L278del/+*, and *L278del/del* animals (Figures S6A and S6D). We assessed whether the reduction in Mast1 protein levels would influence the levels of other MAST family members. Relying on western blot analysis, we observed a striking reduction in the levels of Mast2 and Mast3 in our *L278del* animals (Figures 6A and 6B; n = 4; Mast2: +/+ versus *L278del/+* p < 0.0001; +/+ versus *L278del/del* p < 0.0001; Mast3: +/+ versus *L278del/+* p < 0.0001; +/+ versus *L278del/del* p < 0.0001). This was not attributable to changes in the mRNA levels of *Mast2* and *Mast3*, which were similar in +/+, *L278del/+*, and *L278del/del* animals (Figures S6B and S6C). In contrast, in our *Mast1*

KO animals we observed a significant increase in the levels of Mast2 and Mast3 (Mast2: +/+ versus KO p < 0.0001; Mast3: +/+ versus KO p < 0.001), again with no change in the mRNA levels (Figures S6E and S6F). These data imply that the *L278del* mutation in *Mast1* acts by a dominant-negative mode of action, whereas a form of post-transcriptional compensation occurs in the *Mast1* KO line.

Finally, as previous studies have implicated activation of the PI3K/AKT3/mTOR pathway in corpus callosum hyperplasia associated with megalencephaly, we assessed the phosphorylation state of AKT and rpS6 in our *L278del* mice (Figure 6E) (Broix et al., 2016; Poduri et al., 2012; Rivière et al., 2012; Terrone et al., 2016). We observed no difference in the levels of p-AKT_{S473} and p-rpS6_{S240/244} when comparing heterozygous and homozygous *L278del* brain lysates with wild-type controls (Figure 6F; n = 5 animals; +/+ versus *L278del/+* AKT p > 0.5; +/+ versus *L278del/del* AKT p > 0.5; *L278del/+* versus *L278del/del* AKT p > 0.5; +/+ versus *L278del/+* rpS6 p > 0.5; +/+ versus *L278del/del* rpS6 p > 0.5; *L278del/+* versus *L278del/del* rpS6 p > 0.5).

DISCUSSION

Here, we report that *de novo* mutations in *MAST1* cause MCC-CH-CM, a disease characterized by a striking enlargement of the corpus callosum, cerebellar hypoplasia, and cortical malformations. For patients with this constellation of phenotypes, mutations in *MAST1* appear to be the primary genetic cause, as we observed *MAST1* variants in 6 of the 7 patients that we studied. We have shown that *MAST1* is expressed predominantly in post-mitotic neurons in the developing nervous system, and that it is present in the soma as well as dendritic and axonal compartments. We demonstrate that a *L278del* mouse line recapitulates the enlarged corpus callosum and cerebellar hypoplasia observed in patients, while the *Mast1* KO line lacks any morphological defects. We report extensive cortical apoptosis in our *L278del* mice that is mediated by activated caspases 3 and 9, but not p53 upregulation. We report that this apoptosis varies along the rostro-caudal axis of the cortex, being most severe in caudal regions where the enlarged corpus callosum is least pronounced. Our results show that, unlike other syndromes associated with an enlarged corpus callosum, activation of the PI3K/AKT3/mTOR pathway does not appear to be the underlying pathogenic driver (Terrone et al., 2016).

What molecular mechanism underlies MCC-CH-CM? We have shown that *MAST1* binds to microtubules in a MAP-dependent manner, but this binding is only altered in the case of the K276del mutation. It therefore seems unlikely that alterations in microtubule affinity cause the spectrum of phenotypes we observe in patients with MCC-CH-CM. Analysis of our *L278del* mouse model has shown a dramatic reduction in the levels of Mast2 and Mast3 protein. This result suggests that pathogenic microdeletions in Mast1 act by a dominant-negative mechanism and that the Mast proteins (like other AGC kinases) may physically interact (Leroux et al., 2018). Notably, three of the deletions detected in patients were located in the domain of unknown function (DUF1608), which adopts a 4-helix bundle structure in solution (PDB: 2M9X). Since the helices pack together to form a hydrophobic core, it is expected that the Glu194del,

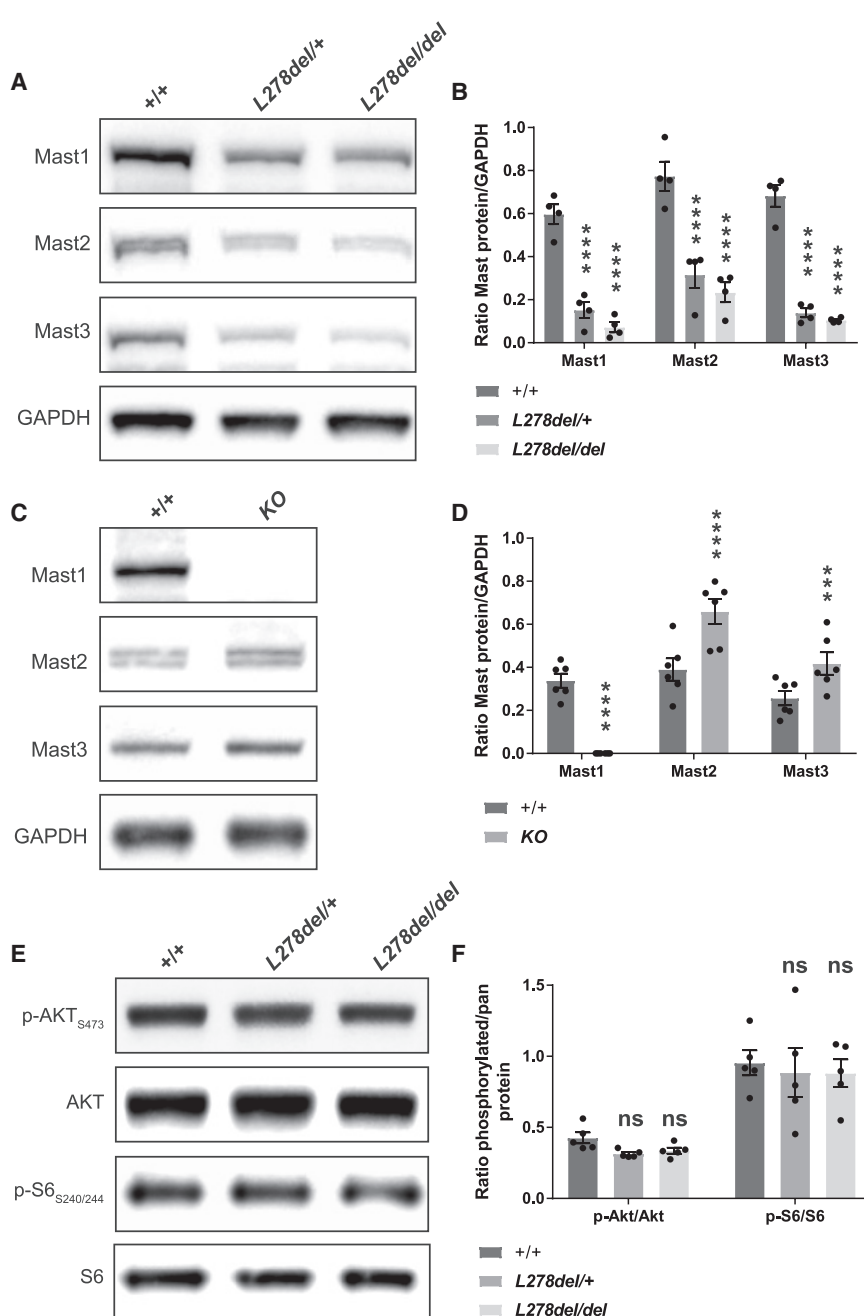


Figure 6. The L278del Mutation Influences Mast1/2/3 Protein Levels but Does Not Activate the PI3K/AKT3/mTOR Pathway

(A and B) Western blot analysis of Mast1, Mast2, and Mast3 on P0 cortical lysates from *L278del* animals. Quantification reveals a dramatic reduction of Mast1, Mast2, and Mast3 protein levels in *L278del* heterozygotes and homozygotes in comparison to littermate controls (n = 4 animals per genotype; two-way repeated-measures ANOVA with a Bonferroni correction). Mast1: +/+ versus *L278del/+* p < 0.0001; +/+ versus *L278del/del* p < 0.0001. Mast2: +/+ versus *L278del/+* p < 0.0001; +/+ versus *L278del/del* p < 0.0001. Mast3: +/+ versus *L278del/+* p < 0.0001; +/+ versus *L278del/del* p < 0.0001. See also Figures S6A–S6C.

(C and D) Western blot analysis of Mast1, Mast2, and Mast3 on brain lysates from *Mast1* KO animals. While Mast1 is absent, there is a significant increase in the levels of Mast2 and Mast3 when compared to littermate controls (n = 6 animals per genotype; two-way repeated-measures ANOVA with a Bonferroni test for multiple comparison). Mast1: +/+ versus KO p < 0.0001. Mast2: +/+ versus KO p < 0.0001. Mast3: +/+ versus KO p < 0.001. See also Figures S6D–S6F.

(E and F) Levels of phosphorylated AKT and ribosomal S6 proteins, indicators of activation of PI3K/AKT/m-TOR pathway, are not significantly different in wild-type and *L278del* P0 cortex (n = 5 animals per genotype; two-way repeated-measures ANOVA with a Bonferroni test for multiple comparison). +/+ versus *L278del/+* AKT p > 0.5; +/+ versus *L278del/del* AKT p > 0.5; *L278del/+* versus *L278del/del* AKT p > 0.5; +/+ versus *L278del/+* rpS6 p > 0.5; +/+ versus *L278del/L278del* rpS6 p > 0.5; *L278del/+* versus *L278del/del* rpS6 p > 0.5.

*p < 0.05; **p < 0.01; ***p < 0.001; ****p < 0.0001. Error bars show mean ± the SEM.

PP2A (Andrade et al., 2017). Mast2 has been reported to interact with $\beta 2$ -syntrophin, but its targets are otherwise undefined (Lumeng et al., 1999). Future experiments that define and validate the targets and binding partners of the MAST family in the developing brain will provide valuable insight on this front.

Why do our *L278del* mice have a thicker corpus callosum? We report that our *L278del* mice present with an enlarged corpus callosum that is most severe in the midbody and genu and manifests despite an increase in cortical apoptosis. Electron microscopic analysis has revealed that this phenotype is not attributable to an increase in the caliber of myelinated neurons, nor to the thickness of the myelin sheath itself, but is associated with an increase in the number of axons that project to the contralateral hemisphere. Such a phenotype may result from: (1) an increase in the branching of callosal fibers, (2) the formation of multiple axons originating from the soma of projection

Lys276del, and Leu278del microdeletions would disrupt this structure by changing the register of the α helices. It is therefore conceivable that these MAST1 microdeletions exert a dominant-negative effect by titrating out functional endogenous MAST proteins and/or targeting them for degradation. The consequence of the reduction in Mast1/2/3 levels is likely to be complex, influencing the phosphorylation of multiple targets. Little is known of the targets of the MAST family; however, Andrade and colleagues have recently shown that in mature dopaminergic neurons in the striatum, MAST3 phosphorylates ARPP-16 at Ser46, which in turn inhibits the serine-threonine phosphatase

neurons, or (3) a change in the fate of differentiating neurons during embryogenesis resulting in an increase in the number of callosal projection neurons at the expense of sub-cortical projection neurons (Baranek et al., 2012; Britanova et al., 2008).

Finally, we report the presence of *de novo* *MAST1* substitutions in patients with severe autism and microcephaly. Notably, a *de novo* P500L mutation in *MAST1* has also been reported in a patient presenting with cerebral palsy (McMichael et al., 2015). This suggests that mutations in *MAST1* give rise to a spectrum of neurodevelopmental diseases. Unlike those mutations that we describe in patients with MCC-CH-CM, these variants are all substitutions, which might account for the different clinical phenotypes. At this stage we are not able to comment on the functional effect of these substitutions, or on the impact of the ~750 coding variants reported in the ExAC control genome database. In light of our work, it is conceivable that mutations in *MAST2* and *MAST3*, both of which are expressed in the developing and adult brain, might also result in neurological disease (Garland et al., 2008). In conclusion, we have defined the genetic lesion that causes MCC-CH-CM and revealed the importance of the *MAST* family in global brain development.

STAR★METHODS

Detailed methods are provided in the online version of this paper and include the following:

- KEY RESOURCES TABLE
- CONTACT FOR REAGENT AND RESOURCE SHARING
- EXPERIMENTAL MODEL AND SUBJECT DETAILS
 - Animals
 - Human studies
 - Cell Lines, primary cultures, microbe strains
- METHOD DETAILS
 - Exome Sequencing
 - qPCR
 - Generation of CRISPR Mice
 - MRI Analysis
 - Electron Microscopy Studies
 - Generation of organoids
 - Nissl Staining and Immunohistochemistry
 - Quantification of Histological Data
 - Immunoblotting
 - Primary neuron culture
 - *In vitro* transcription and translation of Mast1 and microtubule-binding assay
- QUANTIFICATION AND STATISTICAL ANALYSIS
- DATA AND SOFTWARE AVAILABILITY

SUPPLEMENTAL INFORMATION

Supplemental Information includes six figures and four tables and can be found with this article online at <https://doi.org/10.1016/j.neuron.2018.10.044>.

ACKNOWLEDGMENTS

D.A.K. wishes to thank the Austrian Science Foundation (FWF, P21092 and I2681-B27). We wish to acknowledge the support of Boehringer Ingelheim, who fund basic science at the IMP. We wish to thank the CAUSES study,

specifically Shelin Adam, Christele Du Souich, Jane Gillis, Alison Elliott, Anna Lehman, Jill Mwenifumbo, Tanya Nelson, Clara Van Karnebeek, and Jan Friedman. We would also thank Prof. Dr. Bwee Tien Poll and Dr. Saskia Maas for including patient P4 in the study and providing clinical information. T.M.P. is supported by the Diana and Steve Marienhoff Fashion Industries Guild Endowed Fellowship in Pediatric Neuromuscular Diseases. G.M. is generously supported by the National Institute of Neurological Disorders and Stroke (NINDS) (K08NS092898) and Jordan's Guardian Angels. We are indebted to Dr. Vissers for her help with patient P8. J.C.T. and A.T.P. are funded by Oxford NIHR Biomedical Research Centre. N.J.C. acknowledges the support of the NIH (R01GM097376). This work was supported by grants from the Swiss National Science Foundation (31003A_182632) to A.R. G.M.C. and S.M.H. are grateful for support from the National Human Genome Research Institute (UM1HG007301). T.A.L. is funded by the Austrian Science Fund (FWF P28135), and W.B.D. is supported by NIH (1R01NS058721).

AUTHOR CONTRIBUTIONS

Conceptualization: R.T., D.A.K.; Methodology: R.T.; Validation: R.T., M.F.M.-R.; Formal Analysis: R.T., A.W.-W., I.L., M.C.S., L.L.; Visualization: R.T., I.L., M.C.S.; Software: S.L.; Investigation: R.T., I.L., A.W.-W., T.v.D., J.W., B.W.v.B., M.C.S., T.G., M.B., G. Terrone, N.B.-B., A.R.P., A.T.P., G. Tian, G.V., E.D.G., N.B.-P., A.D., N.V., E.F., U.K., T.A.L., S.V., L.A., S.M.H., K.A.A., W.B.D., G.M., M.F.M.-R.; Writing, original draft: R.T., D.A.K; Writing, reviewing, and editing: all authors; Funding acquisition: W.B.D., J.C.T., A.R., J.A.B., L.B., G.M.C., T.M.P., F.B., T.A.L., J.C., N.J.C., D.A.K.; Supervision: J.C.T., A.R., J.A.B., L.B., G.M.C., T.M.P., F.B., J.C., N.J.C., D.A.K.

DECLARATION OF INTERESTS

The authors declare no competing interests.

Received: October 11, 2017

Revised: May 3, 2018

Accepted: October 24, 2018

Published: November 15, 2018

REFERENCES

- Andrade, E.C., Musante, V., Horiuchi, A., Matsuzaki, H., Brody, A.H., Wu, T., Greengard, P., Taylor, J.R., and Naim, A.C. (2017). ARPP-16 Is a Striatal-Enriched Inhibitor of Protein Phosphatase 2A Regulated by Microtubule-Associated Serine/Threonine Kinase 3 (Mast 3 Kinase). *J. Neurosci.* 37, 2709–2722.
- Baranek, C., Dittrich, M., Parthasarathy, S., Bonnon, C.G., Britanova, O., Lanshakov, D., Boukhtouche, F., Sommer, J.E., Colmenares, C., Tarabykin, V., and Atanasoski, S. (2012). Protooncogene Ski cooperates with the chromatin-remodeling factor Satb2 in specifying callosal neurons. *Proc. Natl. Acad. Sci. USA* 109, 3546–3551.
- Braun, A., Breuss, M., Salzer, M.C., Flint, J., Cowan, N.J., and Keays, D.A. (2010). Tuba8 is expressed at low levels in the developing mouse and human brain. *Am. J. Hum. Genet.* 86, 819–822, author reply 822–823.
- Breuss, M., Morandell, J., Nimpf, S., Gstrein, T., Lauwers, M., Hochstoeger, T., Braun, A., Chan, K., Sánchez Guajardo, E.R., Zhang, L., et al. (2015). The expression of Tubb2b undergoes a developmental transition in murine cortical neurons. *J. Comp. Neurol.* 523, 2161–2186.
- Breuss, M., Fritz, T., Gstrein, T., Chan, K., Ushakova, L., Yu, N., Vonberg, F.W., Werner, B., Elling, U., and Keays, D.A. (2016). Mutations in the murine homologue of TUBB5 cause microcephaly by perturbing cell cycle progression and inducing p53-associated apoptosis. *Development* 143, 1126–1133.
- Britanova, O., de Juan Romero, C., Cheung, A., Kwan, K.Y., Schwark, M., Gyorgy, A., Vogel, T., Akopov, S., Mitkovski, M., Agoston, D., et al. (2008). Satb2 is a postmitotic determinant for upper-layer neuron specification in the neocortex. *Neuron* 57, 378–392.
- Broix, L., Jagline, H., Ivanova, E., Schmucker, S., Drouot, N., Clayton-Smith, J., Pagnamenta, A.T., Metcalfe, K.A., Isidor, B., Louvier, U.W., et al.;

- Deciphering Developmental Disorders study (2016). Mutations in the HECT domain of NEDD4L lead to AKT-mTOR pathway deregulation and cause periventricular nodular heterotopia. *Nat. Genet.* 48, 1349–1358.
- Cingolani, P., Platts, A., Wang, L., Coon, M., Nguyen, T., Wang, L., Land, S.J., Lu, X., and Ruden, D.M. (2012). A program for annotating and predicting the effects of single nucleotide polymorphisms, SnpEff: SNPs in the genome of *Drosophila melanogaster* strain w1118; iso-2; iso-3. *Fly (Austin)* 6, 80–92.
- GTEx Consortium (2013). The Genotype-Tissue Expression (GTEx) project. *Nat. Genet.* 45, 580–585.
- Cubelos, B., Briz, C.G., Esteban-Ortega, G.M., and Nieto, M. (2015). Cux1 and Cux2 selectively target basal and apical dendritic compartments of layer II-III cortical neurons. *Dev. Neurobiol.* 75, 163–172.
- Demyanenko, G.P., Tsai, A.Y., and Maness, P.F. (1999). Abnormalities in neuronal process extension, hippocampal development, and the ventricular system of L1 knockout mice. *J. Neurosci.* 19, 4907–4920.
- DePristo, M.A., Banks, E., Poplin, R., Garimella, K.V., Maguire, J.R., Hartl, C., Philippakis, A.A., del Angel, G., Rivas, M.A., Hanna, M., et al. (2011). A framework for variation discovery and genotyping using next-generation DNA sequencing data. *Nat. Genet.* 43, 491–498.
- DiMario, F.J., Jr., Ramsby, G.R., and Burleson, J.A. (1999). Brain morphometric analysis in neurofibromatosis 1. *Arch. Neurol.* 56, 1343–1346.
- Edwards, T.J., Sherr, E.H., Barkovich, A.J., and Richards, L.J. (2014). Clinical, genetic and imaging findings identify new causes for corpus callosum development syndromes. *Brain* 137, 1579–1613.
- Ferland, R.J., Cherry, T.J., Prewar, P.O., Morrisey, E.E., and Walsh, C.A. (2003). Characterization of Foxp2 and Foxp1 mRNA and protein in the developing and mature brain. *J. Comp. Neurol.* 460, 266–279.
- Garland, P., Quraishe, S., French, P., and O'Connor, V. (2008). Expression of the MAST family of serine/threonine kinases. *Brain Res.* 1195, 12–19.
- Gilissen, C., Hehir-Kwa, J.Y., Thung, D.T., van de Vorst, M., van Bon, B.W., Willemsen, M.H., Kwint, M., Janssen, I.M., Hoischen, A., Schenck, A., et al. (2014). Genome sequencing identifies major causes of severe intellectual disability. *Nature* 511, 344–347.
- Göhlich-Ratmann, G., Baethmann, M., Lorenz, P., Gärtner, J., Goebel, H.H., Engelbrecht, V., Christen, H.J., Lenard, H.G., and Voit, T. (1998). Megalencephaly, mega corpus callosum, and complete lack of motor development: a previously undescribed syndrome. *Am. J. Med. Genet.* 79, 161–167.
- Guy, J., Ellis, E.A., Kelley, K., and Hope, G.M. (1989). Spectra of G ratio, myelin sheath thickness, and axon and fiber diameter in the guinea pig optic nerve. *J. Comp. Neurol.* 287, 446–454.
- Hengst, M., Tücke, J., Zerres, K., Blaum, M., and Häusler, M. (2010). Megalencephaly, mega corpus callosum, and complete lack of motor development: delineation of a rare syndrome. *Am. J. Med. Genet. A.* 152A, 2360–2364.
- Hyman, B.T., and Yuan, J. (2012). Apoptotic and non-apoptotic roles of caspases in neuronal physiology and pathophysiology. *Nat. Rev. Neurosci.* 13, 395–406.
- Iyer, V., Shen, B., Zhang, W., Hodgkins, A., Keane, T., Huang, X., and Skarnes, W.C. (2015). Off-target mutations are rare in Cas9-modified mice. *Nat. Methods* 12, 479.
- Johannessen, C.M., Reczek, E.E., James, M.F., Brems, H., Legius, E., and Cichowski, K. (2005). The NF1 tumor suppressor critically regulates TSC2 and mTOR. *Proc. Natl. Acad. Sci. USA* 102, 8573–8578.
- Keays, D.A., Tian, G., Poirier, K., Huang, G.J., Siebold, C., Cleak, J., Oliver, P.L., Fray, M., Harvey, R.J., Molnár, Z., et al. (2007). Mutations in alpha-tubulin cause abnormal neuronal migration in mice and lissencephaly in humans. *Cell* 128, 45–57.
- Kenna, K.P., van Doornmaal, P.T., Dekker, A.M., Ticozzi, N., Kenna, B.J., Diekstra, F.P., van Rheenen, W., van Eijk, K.R., Jones, A.R., Keagle, P., et al.; SLAGEN Consortium (2016). NEK1 variants confer susceptibility to amyotrophic lateral sclerosis. *Nat. Genet.* 48, 1037–1042.
- Kircher, M., Witten, D.M., Jain, P., O'Roak, B.J., Cooper, G.M., and Shendure, J. (2014). A general framework for estimating the relative pathogenicity of human genetic variants. *Nat. Genet.* 46, 310–315.
- Korogod, N., Petersen, C.C., and Knott, G.W. (2015). Ultrastructural analysis of adult mouse neocortex comparing aldehyde perfusion with cryo fixation. *eLife* 4, <https://doi.org/10.7554/eLife.05793>.
- Kosik, K.S., and Finch, E.A. (1987). MAP2 and tau segregate into dendritic and axonal domains after the elaboration of morphologically distinct neurites: an immunocytochemical study of cultured rat cerebrum. *J. Neurosci.* 7, 3142–3153.
- Lancaster, M.A., and Knoblich, J.A. (2014). Generation of cerebral organoids from human pluripotent stem cells. *Nat. Protoc.* 9, 2329–2340.
- Lancaster, M.A., Renner, M., Martin, C.A., Wenzel, D., Bicknell, L.S., Hurles, M.E., Homfray, T., Penninger, J.M., Jackson, A.P., and Knoblich, J.A. (2013). Cerebral organoids model human brain development and microcephaly. *Nature* 501, 373–379.
- Lek, M., Karczewski, K.J., Minikel, E.V., Samocha, K.E., Banks, E., Fennell, T., O'Donnell-Luria, A.H., Ware, J.S., Hill, A.J., Cummings, B.B., et al.; Exome Aggregation Consortium (2016). Analysis of protein-coding genetic variation in 60,706 humans. *Nature* 536, 285–291.
- Leroux, A.E., Schulze, J.O., and Biondi, R.M. (2018). AGC kinases, mechanisms of regulation and innovative drug development. *Semin. Cancer Biol.* 48, 1–17.
- Li, H., and Durbin, R. (2010). Fast and accurate long-read alignment with Burrows-Wheeler transform. *Bioinformatics* 26, 589–595.
- Lumeng, C., Phelps, S., Crawford, G.E., Walden, P.D., Barald, K., and Chamberlain, J.S. (1999). Interactions between beta 2-syntrophin and a family of microtubule-associated serine/threonine kinases. *Nat. Neurosci.* 2, 611–617.
- Marsh, A.P., Heron, D., Edwards, T.J., Quartier, A., Galea, C., Nava, C., Rastetter, A., Moutard, M.L., Anderson, V., Bitoun, P., et al. (2017). Mutations in DCC cause isolated agenesis of the corpus callosum with incomplete penetrance. *Nat. Genet.* 49, 511–514.
- McKenna, A., Hanna, M., Banks, E., Sivachenko, A., Cibulskis, K., Kernytsky, A., Garimella, K., Altshuler, D., Gabriel, S., Daly, M., and DePristo, M.A. (2010). The Genome Analysis Toolkit: a MapReduce framework for analyzing next-generation DNA sequencing data. *Genome Res.* 20, 1297–1303.
- McMichael, G., Bainbridge, M.N., Haan, E., Corbett, M., Gardner, A., Thompson, S., van Bon, B.W., van Eyk, C.L., Broadbent, J., Reynolds, C., et al. (2015). Whole-exome sequencing points to considerable genetic heterogeneity of cerebral palsy. *Mol. Psychiatry* 20, 176–182.
- Meixner, A., Haverkamp, S., Wässle, H., Führer, S., Thalhammer, J., Kropf, N., Bittner, R.E., Lassmann, H., Wiche, G., and Propst, F. (2000). MAP1B is required for axon guidance and is involved in the development of the central and peripheral nervous system. *J. Cell Biol.* 151, 1169–1178.
- Morris, J.A., Royall, J.J., Bertagnoli, D., Boe, A.F., Burnell, J.J., Byrnes, E.J., Copeland, C., Desta, T., Fischer, S.R., Goldy, J., et al. (2010). Divergent and nonuniform gene expression patterns in mouse brain. *Proc. Natl. Acad. Sci. USA* 107, 19049–19054.
- Nguyen, L.S., Schneider, T., Rio, M., Moutton, S., Siquier-Pernet, K., Verny, F., Boddaert, N., Desguerre, I., Munich, A., Rosa, J.L., et al. (2016). A nonsense variant in HERC1 is associated with intellectual disability, megalencephaly, thick corpus callosum and cerebellar atrophy. *Eur. J. Hum. Genet.* 24, 455–458.
- Niquille, M., Garel, S., Mann, F., Hornung, J.P., Otsmane, B., Chevally, S., Parras, C., Guillemot, F., Gaspar, P., Yanagawa, Y., and Lebrand, C. (2009). Transient neuronal populations are required to guide callosal axons: a role for semaphorin 3C. *PLoS Biol.* 7, e1000230.
- Parrini, E., Conti, V., Dobyns, W.B., and Guerrini, R. (2016). Genetic Basis of Brain Malformations. *Mol. Syndromol.* 7, 220–233.
- Paul, L.K., Brown, W.S., Adolphs, R., Tyszka, J.M., Richards, L.J., Mukherjee, P., and Sherr, E.H. (2007). Agenesis of the corpus callosum: genetic,

- developmental and functional aspects of connectivity. *Nat. Rev. Neurosci.* 8, 287–299.
- Paxinos, G.H.G., Watson, C., Koutcherov, Y., and Wang, H. (2007). *Atlas of the Developing Mouse Brain* (Academic Press).
- Pierson, T.M., Zimmerman, R.A., Tennekoon, G.I., and Bönnemann, C.G. (2008). Mega-corpus callosum, polymicrogyria, and psychomotor retardation: confirmation of a syndromic entity. *Neuropediatrics* 39, 123–127.
- Poduri, A., Ervony, G.D., Cai, X., Elhosary, P.C., Beroukhim, R., Lehtinen, M.K., Hills, L.B., Heinzen, E.L., Hill, A., Hill, R.S., et al. (2012). Somatic activation of AKT3 causes hemispheric developmental brain malformations. *Neuron* 74, 41–48.
- Rivière, J.B., Mirzaa, G.M., O'Roak, B.J., Beddaoui, M., Alcantara, D., Conway, R.L., St-Onge, J., Schwartzenbuber, J.A., Gripp, K.W., Nikkel, S.M., et al.; Finding of Rare Disease Genes (FORGE) Canada Consortium (2012). De novo germline and postzygotic mutations in AKT3, PIK3R2 and PIK3CA cause a spectrum of related megalencephaly syndromes. *Nat. Genet.* 44, 934–940.
- Serafini, T., Colamarino, S.A., Leonardo, E.D., Wang, H., Beddington, R., Skarnes, W.C., and Tessier-Lavigne, M. (1996). Netrin-1 is required for commissural axon guidance in the developing vertebrate nervous system. *Cell* 87, 1001–1014.
- Sobreira, N., Schiettecatte, F., Valle, D., and Hamosh, A. (2015). GeneMatcher: a matching tool for connecting investigators with an interest in the same gene. *Hum. Mutat.* 36, 928–930.
- Sturrock, R.R. (1980). Myelination of the mouse corpus callosum. *Neuropathol. Appl. Neurobiol.* 6, 415–420.
- Szybińska, A., and Leśniak, W. (2017). P53 Dysfunction in Neurodegenerative Diseases - The Cause or Effect of Pathological Changes? *Aging Dis.* 8, 506–518.
- Terrone, G., Voisin, N., Abdullah Alfaiz, A., Cappuccio, G., Vitiello, G., Guex, N., D'Amico, A., James Barkovich, A., Brunetti-Pierri, N., Del Giudice, E., and Reymond, A. (2016). De novo PIK3R2 variant causes polymicrogyria, corpus callosum hyperplasia and focal cortical dysplasia. *Eur. J. Hum. Genet.* 24, 1359–1362.
- Thiel, C., Kessler, K., Giessl, A., Dimmeler, A., Shalev, S.A., von der Haar, S., Zenker, M., Zahnleiter, D., Stöss, H., Beinder, E., et al. (2011). NEK1 mutations cause short-rib polydactyl syndrome type majewski. *Am. J. Hum. Genet.* 88, 106–114.
- Tischfield, M.A., Baris, H.N., Wu, C., Rudolph, G., Van Maldergem, L., He, W., Chan, W.M., Andrews, C., Demer, J.L., Robertson, R.L., et al. (2010). Human TUBB3 mutations perturb microtubule dynamics, kinesin interactions, and axon guidance. *Cell* 140, 74–87.
- Walden, P.D., and Cowan, N.J. (1993). A novel 205-kilodalton testis-specific serine/threonine protein kinase associated with microtubules of the spermatid manchette. *Mol. Cell. Biol.* 13, 7625–7635.
- Wang, H., Yang, H., Shivalila, C.S., Dawlaty, M.M., Cheng, A.W., Zhang, F., and Jaenisch, R. (2013). One-step generation of mice carrying mutations in multiple genes by CRISPR/Cas-mediated genome engineering. *Cell* 153, 910–918.
- West, K.L., Kelm, N.D., Carson, R.P., and Does, M.D. (2015). Quantitative analysis of mouse corpus callosum from electron microscopy images. *Data Brief* 5, 124–128.

STAR★METHODS

KEY RESOURCES TABLE

REAGENT or RESOURCE	SOURCE	IDENTIFIER
Antibodies		
anti-Mast1	Santa Cruz	Cat#sc-55851; RRID:AB_2141214
anti-Mast1 (G-4)	Santa Cruz	Cat#sc-373845; RRID:AB_10988599
anti-Tbr2	Abcam	Cat#ab23345; RRID:AB_778267
anti-Pax6	Covance	Cat#PRB-278P; RRID:AB_291612
anti-Tuj1	Covance	Cat#MMS-435P; RRID:AB_2313773
anti-Cux1	Santa Cruz	Cat#sc-6327; RRID:AB_2087003
anti-NeuN (A60)	Millipore	Cat#MAB377; RRID:AB_2298772
anti-Er81	Abcam	Cat#ab36788; RRID:AB_732196
anti-Foxp2	Abcam	Cat#ab16046; RRID:AB_2107107
anti-Olig2	Millipore	Cat#AB9610; RRID:AB_570666
anti-GFAP	Dako	Cat# Z0334; RRID: AB_2314535
anti-Map2	Abcam	Cat#AB24640; RRID:AB_448205
anti-Tau	Abcam	Cat#AB64193; RRID:AB_1143333
anti-cleaved-Caspase-3	Cell Signaling Technology	Cat#9661; RRID:AB_2341188
anti-cleaved-Caspase-9	Cell Signaling Technology	Cat#9509; RRID:AB_2073476
anti-p53	Leica	Cat#P53-CM5P; RRID:AB_2744683
anti-Calbindin	Millipore	Cat#AB1778; RRID:AB_2068336
anti-Mast1	Proteintech	Cat#13305-1-AP; RRID:AB_10639043
anti-Mast2	Santa Cruz	Cat#sc-377198; RRID:AB_2744682
anti-Mast3	Novus	Cat#NBP1-82993; RRID:AB_11017204
anti-p-Akt(Ser473)	Cell Signaling Technology	Cat#4060; RRID:AB_2315049
anti-Akt	Cell Signaling Technology	Cat#9272; RRID:AB_329827
anti-p-S6(Ser240/244)	Cell Signaling Technology	Cat#2215; RRID:AB_2630325
anti-S6	Cell Signaling Technology	Cat#5548; RRID:AB_10707322
anti-GAPDH	Millipore	Cat#MAB374; RRID:AB_2107445
Bacterial and Virus Strains		
<i>E. coli</i> DH5alpha	Invitrogen	Cat#18265017
Experimental Models: Cell Lines		
H9 feeder free hES cells	WiCell, University of Wisconsin	WA09
Experimental Models: Organisms/Strains		
Leu278del	this paper	N/A
Mast1 knockout line5	this paper	N/A
Mast1 knockout line31	this paper	N/A
Tubb5 flx	In house	MGI Cat# 6119480, RRID:MGI:6119480
Nestin Cre	In house	IMSR Cat# JAX:019103, RRID:IMSR_JAX:019103
Oligonucleotides		
GCAAGGTGTACAGCAGTATGG	sigma	mMAST1_qPCR_F
TGGGTCCCGCTTGCTG	sigma	mMAST1_qPCR_R
GGTGCATCTGGAGGAACAG	sigma	hMAST1_qPCR _F
GATGGTATCGAAGTCATTCTCCC	sigma	hMAST1_qPCR _R
AAGGTTCAAGGTTACAGTAG	sigma	mMAST2_qPCR_F
AAGCCGTCTGAGTGATCTC	sigma	mMAST2_qPCR_R

(Continued on next page)

Continued

REAGENT or RESOURCE	SOURCE	IDENTIFIER
AAGATGGTCACTTGCTTCC	sigma	mMAST3_qPCR_F
AGGACGAGCTTGACGATAC	sigma	mMAST3_qPCR_R
TAATCATCTCGCCCTGCA	sigma	mMast1_ex8_gRNA2
GGAGAGGGTCTTACTGCTT	sigma	mMast1_ex8_mutscrn_F
TCTTCTGGGTTGAATTCTTA	sigma	mMast1_ex8_mutscrn_R
Recombinant DNA		
pcDNA3.1-5'UTRmMast1-E194del	this paper	N/A
pcDNA3.1-5'UTRmMast1-K276del	this paper	N/A
pcDNA3.1-5'UTRmMast1-L278del	this paper	N/A
pcDNA3.1-5'UTRmMast1-G519S	this paper	N/A
Software and Algorithms		
ImageJ	open source (at NIH)	N/A
GraphPad prism v.7	GraphPad Software	N/A

CONTACT FOR REAGENT AND RESOURCE SHARING

Further information and requests for resources and reagents should be directed to and will be fulfilled by the lead contact, Dr. David Keays (david.keays@imp.ac.at).

EXPERIMENTAL MODEL AND SUBJECT DETAILS

Animals

Mice were maintained on a 12:12 light dark cycle and food was available *ad libitum*. Mice of ages E10.5, E12.5, E14.5, E16.5, P0, P6, 8–10 weeks were used in this study. Animals were not subject to randomization and allocated to experimental groups according to their genotypes as littermates regardless of the sex. For experiments with mice of ages E10.5, E12.5, E14.5, E16.5, P0, P6 the sex was not determined. For generating CRISPR mouse lines, female BL6/CBA F1 mice were used, whereas all backcrosses were performed using C57/BL6 mice to the 7th generation. All procedures were carried out according to legal requirements and covered by an approved license (M58/006093/2011/14).

Human studies

Informed consent was obtained from all patients included in this study. Details of each patient and the condition is provided in [Tables 1](#) and [S1](#). This study was conducted within approved ethical frameworks University of Oxford (08/MRE09/55); Stanford University Institutional Review Board (28362); University of Alabama at Birmingham (X130201001); and at the Seattle Children's Research Institute (IRB protocol #13291); and by the Commissie Mensgebonden Onderzoek Regio Arnhem-Nijmegen (NL36191.091.11).

Cell Lines, primary cultures, microbe strains

For generating cerebral organoids, feeder free H9 human embryonic stem cells (ESCs) were obtained from Wicell (WA09), having a normal karyotype, female sex, and no contaminants. These cells were maintained using the commercially available mTESR media (Stem cell technologies #05850) at 37°C with 5% CO₂ levels. These cells were not authenticated. Primary cell cultures were generated from P0 and P7 cortex or cerebellum. The sex of these pups was not determined. The primary neurons were cultured in Neurobasal media with B27, Penstrep and L-glutamine supplements at 37°C with 5% CO₂ levels. The *Escherichia coli* DH5alpha strain was used for cloning purposes.

METHOD DETAILS

Exome Sequencing

Patients with structural brain phenotypes and their parents were recruited in accordance with existing ethical frameworks and internal review boards. DNA from blood was extracted using standard methods and subject to exome sequencing. We exploited capture arrays (such as the Agilent Human All exon 50Mb array) to capture exonic genomic DNA, which was then subject to next generation paired end sequencing (Illumina). Bioinformatic filtering employed platforms such as the Genome Analysis Toolkit (GATK), and excluded variants with a population frequency greater than 1%. For this purpose, we relied on available genomic databases including dbSNP and the 1000 Genomes server. Sanger sequencing was employed to confirm any putative *de novo* variants. This study was

conducted within an approved ethical framework (08/MRE09/55). For mouse exome sequencing genomic DNA was extracted from the tails of BL6J, CBA, and L278del mice and then subjected to Illumina library preparation and captured on the Agilent SureSelect mouse (51Mb) array. The samples were sequenced on an Illumina HiSeq2500 with 100-125 nucleotides paired-end reads followed by data quality analysis using FASTQC. Reads were mapped to the mouse genome (GRCm38, mm10) using BWA (Li and Durbin, 2010). The BAM files were used as an input to UnifiedGenotyper module from the GATK-lite toolkit (v2.3). (McKenna et al., 2010) Variants were called and dbSNP variants were used as known sites, according to GATK Best Practices recommendations (DePristo et al., 2011). Finally, Variants were annotated by SnpEff v4.1 (Cingolani et al., 2012). Sanger sequencing was employed to confirm putative *de novo* variants on chromosome 8, potentially linked to the L278del mutation (Table S2).

qPCR

The following tissues were dissected from C57/BL6 mice: embryonic brains at stages E10.5, E12.5, E14.5, E16.5, E18.5 (undetermined sex); brains from early postnatal mice at P0, P6 (undetermined sex); the brain regions (cortex, cerebellum, hippocampus, striatum, midbrain, colliculi, hypothalamus, brain stem, spinal cord, olfactory bulbs) and organs (liver, spleen, heart, muscle, testis, kidney, lung) from male adult littermates ($n = 3$). To ascertain Mast1, Mast2, and Mast3 mRNA levels in L278del and KO animals, cortices from littermate homozygote, heterozygote, and wild-type P0s were obtained (undetermined sex) ($n = 4$). Tissue samples were snap frozen before total RNA extraction and cDNA synthesis (SuperScript III First-Strand Synthesis System, Invitrogen, 18080-051). We used SYBR green on a Bio-Rad Cycler together with intro spanning primers to amplify murine Mast1 (mMAST1_qPCR_F/GCAAGGTGTAC AGCAGTATGG, mMAST1_qPCR_R/TGGGTCCCGCTTGCTG). For qPCR on human fetal tissue (hMAST1_qPCR_F/GGTGCATCT GGAGGAACAG, hMAST1_qPCR_R/GATGGTATCGAAGTCATTCTCCC) we performed technical triplicates on two different cDNA libraries (Biochain; C1244051, C1244035) again using intro spanning primers. In addition, we amplified three control genes (Pgk1, Tfrc, and Hprt). For each control gene technical triplicates were performed, and the geometric mean of the Ct values for the three control genes calculated. This geometric mean was then used to obtain the delta Ct value by subtracting it from the average (of triplicate runs) Ct value for Mast1. The relative mRNA levels were then obtained by taking into account the efficiency of the qPCR primers (see Braun et al., 2010).

Generation of CRISPR Mice

Female BL6/CBA F1 mice (3–4 weeks old) were superovulated according to standard protocols. Zygotes were isolated from donor females at the day of the coagulation plug (= E0.5). Surrounding cumulus cells were removed by incubation of the cumulus-zygote-complexes in hyaluronidase solution (at ~0.3 mg/mL). The injection mix (50 ng/μL Cas9 mRNA + 50 ng/μL guide RNA + 200 ng/μL L278del-ssODN repair template) was injected into the cytoplasm of zygotes. Injected zygotes were incubated for at least 15 min in a CO₂ incubator at 37°C. Zygotes that survived microinjection were transferred the same day into the oviducts of pseudopregnant recipient females (= 0.5 days post coitum). Resultant pups were genotyped by PCR amplification of chromosome 8 followed by sequencing using primers GGAGAGGGTCTTACTTGCTT and TCTTCTGGGTTGAATTCTTA, and backcrossed to C57/BL6.

MRI Analysis

MRI analysis was performed as described previously (Breuss et al., 2016). Briefly, 8-week old littermates were perfused with 0.9% NaCl and 4% PFA supplemented with 10% ProHance Solution (Bracco Imaging Group, 4002750). Images were then acquired with a 15.2 T Biospec horizontal bore scanner (Bruker BioSpin, Ettlingen, Germany). Brain regions of interest were manually segmented, blinded to the genotype, using Amira 5.6 (Visualization Science Group), relying on a mouse brain atlas, and the volumes obtained.

Electron Microscopy Studies

Mice aged 8–9 weeks ($n = 5$) were sacrificed and brain tissue prepared for electron microscopy (Korogod et al., 2015). Briefly, animals were perfused employing a constant flow of 7 mL/min with 2.5% glutaraldehyde and 2% paraformaldehyde in phosphate buffer (0.1 M, pH 7.4). Following dissection of the brain, 80-μm thick coronal slices were prepared on a vibratome (Leica VT 1000S). Matching slices were selected from the medial region of each brain (bregma –0.10), the corpus callosum microdissected, and then post fixed for 40 min in 1% osmium tetroxide in cacodylate buffer (0.1 M, pH 7.4). Samples were then washed twice for 5 min in ddH₂O and stained with 1% uranyl acetate for 40 min before being dehydrated in a graded acetone series and embedded in Epon resin. Ultrathin sections were prepared (70nm), mounted on 50 mesh grids and post-stained with uranyl acetate (10 min, 2% in water) and with Reynolds' lead citrate (5 min). To assess differences in myelin thickness and axon, internal diameter images were captured at 8900x using a FEI Morgagni 268D (FEI Company) 100 kV transmission electron microscope operating at 80 kV. A customized script written in Definiens Architect XD (Version: 2.7.0; Build 60765X64) was employed to ascertain axonal surface area and myelin thickness determined using ImageJ. To ascertain the number of axons crossing the midline, images were acquired at 710x along the dorsa-ventral axis. These images (approx 10–12) per animal were then tiled employing iTEM, resulting in a single image. A box measuring 30 μm along the x axis was then overlaid onto the structure, and the total number of myelinated axons counted manually. Three stitched images were prepared per animal and all analysis was performed blind to genotype. To determine the G-ratio of axons crossing the midline we measured the total diameter of fibers (> 300 per animal) and the axonal diameter (without myelin) on high resolution EM images. The G-ratio was then calculated (axon diameter/fiber diameter) (Guy et al., 1989).

Generation of organoids

Human cerebral organoids were generated from H9 human ESCs (Wicell, WA09) as previously described (Lancaster and Knoblich, 2014) ENREF_14. 64 days-old organoids were then embedded in Neg-50 Medium (Richard-Allan Scientific) and sliced into 20 μm sections in a cryostat. The slides were dried overnight before storing at -20°C and stained as described below.

Nissl Staining and Immunohistochemistry

Brains were removed at E12.5, E14.5, E16.5, E18.5, P0 and drop-fixed in 4% PFA overnight followed by dehydration in 30% sucrose. Brains were embedded in Neg-50 Medium (Richard-Allan Scientific) and sliced into 12 μm sections in a cryostat. Adults brains were recovered from the animals after perfusion with 0.9% NaCl and 4% PFA. These brains were post-fixed, dehydrated, and sliced using a sledge microtome into 40 μm sections. For Nissl staining, sections were washed in PBS, and bathed in Cresyl Violet for 3 min [0.25% Cresyl Violet acetate (Sigma, C5042) dissolved in distilled water with ten drops of glacial acetic acid per 100 mL of solution]. After briefly washing in PBS, slides were dehydrated in an alcohol series (30%, 70%, 96% and 100% ethanol, 2 min each), xylol (twice, 2 min each), mounted with DPX mountant (Fluka, 44581) and left overnight at room temperature. Images were acquired using the transmitted Mirax slide scanner (Zeiss).

Immunofluorescence experiments were performed as previously described (Breuss et al., 2016; Breuss et al., 2015). Where necessary antigen retrieval was performed on sections by slow heating of the slides in antigen retrieval buffer (Vector, H-3301) up to 90°C , followed by gradual cooling at room temperature for 20 min. Primary antibody in 0.1%–0.3% Triton X-100/PBS with 4% donkey serum as the blocking agent, was incubated overnight at 4°C . The following concentrations of primary antibodies were used: 1:300 Mast1 (Santa Cruz, sc-55851), 1:100 Mast1 (Santa Cruz, sc-373845) 1:300 cleaved-Caspase-3 (Cell Signaling, #9661), 1:300 cleaved-Caspase-9 (Cell Signaling #9509), 1:300 Pax6 (Covance, PRB-278P), 1:300 Tbr2 (Abcam, ab23345), 1:1000 Tuj (Covance, MMS-435P), 1:300 NeuN (Millipore, MAB377), 1:100 Cux1 (Santa Cruz, sc-6327), 1:1000 Er81 (Abcam, ab36788), 1:300 FoxP2 (Abcam, ab16046), 1:250 Calbindin (Millipore, AB1778), 1:1000 Olig2 (Millipore, AB9610), GFAP 1:500 (Dako, Z0334), 1:300 Map2 (Abcam, ab24640), 1:300 Tau (Abcam, ab61493), 1:1000 p53 (Leica, P53-CM5P). The next day, sections were washed in PBS and a species-specific secondary antibody (Molecular Probes, A-10037, A-11057, A-10042, A-21206; 1:500) was applied for 1 h in blocking solution at 4°C , followed by Hoechst 33342 staining (1:2000 in PBS) for 5 min. Subsequently the slides were mounted with Fluorescent Mounting Medium (Dako, S302380) and dried overnight at 4°C before imaging. Images were taken using a laser scanning confocal microscope (LSM 780 Zeiss).

Quantification of Histological Data

To determine the thickness of the corpus callosum in Nissl-stained sections the septum in the genu region was measured three times and an average determined (bregma co-ordinates 0.86mm). To determine the cortical thickness six measurements were obtained for rostral (bregma co-ordinates 0.86 mm) and caudal regions (bregma co-ordinates –1.82mm) and averaged for each animal. To assess the thickness of various cortical layers, matched caudal immunostained (Foxp2, Cux1, Er81) sections were measured four times in the region of the somatosensory cortex and averaged for each animal. To assess the levels of apoptosis in the cortex of P0 animals caspase-3 and caspase-9-positive puncta were counted in 3 matched sections (spanning anatomical co-ordinates 3.75mm to 4.0mm [Paxinos et al., 2007]), and the number averaged per animal. To compare rostral and caudal cortical apoptosis at P0 caspase-3 positive punctae were counted in a box measuring $1000 \times 300 \mu\text{m}^2$, in rostral sections ($n = 2$ sections per animal, co-ordinates 2.3–2.5mm [Paxinos et al., 2007]) and caudal sections ($n = 2$ sections per animal, co-ordinates: 3.75–4.0mm [Paxinos et al., 2007]). To assess levels of apoptosis in the P0 cerebellum, caspase-3-positive puncta were counted in 2 matched sections per animal (spanning anatomical co-ordinates 7mm to 7.25mm [Paxinos et al., 2007]) and the number averaged per section. To quantify the number and density of oligodendrocytes and astrocytes within the corpus callosum coronal sections from 8 week old animals were stained with Olig2 and GFAP. A box measuring 770 μm wide was placed over the septum of the corpus callosum extending from the ventral to dorsal edges, and positively stained cells were manually counted. To quantitate the number of Purkinje and granule cells in the cerebellum, free-floating, 40 μm , sagittal midline cerebellar sections were stained with anti-sera for Calbindin and NeuN, followed by counterstaining with DAPI ($n = 2$ sections per animal). Folium III was imaged and all Purkinje cells in this folium were counted allowing determination of the Purkinje cell linear density (cells/mm of Purkinje cell layer). The total number of Purkinje cells per section was then estimated by measuring the entire length of the Purkinje cell layer. To estimate the number of granule cells per section 4 images per animal were captured within the granule cell layer of folium III, and the density of granule cells/mm 2 of granule layer (GL) was determined. The total number of cells per section was then estimated by measuring the entire surface area of the GL and multiplying it by the average density for that animal. All quantifications were done using ImageJ software and performed blinded to the genotype.

Immunoblotting

Brains were snap frozen in liquid nitrogen and stored at -80°C . Protein lysates were prepared from frozen tissue samples, homogenized in chilled lysis buffer (20 mM TrisHCl pH 7.5, 100 mM NaCl, 10% glycerol, 1% Triton X-100) supplemented with protease and phosphatase inhibitors (Pierce #88668). Using a Tungsten Carbide Bead the tissue was lysed in a QIAGEN Tissue Lyser (2 \times 1 min, 20Hz), incubated at 4°C for 1 hr, and then centrifuged twice for 20 min. Protein concentration of the collected supernatant was measured using the Pierce BCA Protein Assay Kit (#23225). Protein lysates were run on NuPAGE protein gels, blotted onto

nitrocellulose membranes and blocked in 5% skimmed milk/TBST. Primary antibodies [1:2000 GAPDH (Millipore, MAB374); 1:1000 Mast1 (Proteintech, 13305-1-AP); 1:300 Mast2 (Santa Cruz, sc-377198); 1:500 Mast3 (Novus; NBP1-82993); 1:1000 pan-Akt (Cell Signaling Technology #9272); 1:1000 Phospho-Akt (Ser473) (Cell Signaling Technology #4060); 1:500 S6 Ribosomal Protein (Cell Signaling Technology #5548); 1:1000 Phospho-S6 Ribosomal Protein (Ser240/244) (Cell Signaling Technology #2215)] were incubated overnight in blocking solution at 4°C. The following day, the blot was incubated with the corresponding HRP conjugated secondary antibody (abcam) for 1 hr at room temperature. The signal was detected on Amersham Hyperfilm ECL film using the ECL Western Blotting Detection Reagents kit (GE healthcare, RPN2106). Western blots were quantified using ImageJ.

Primary neuron culture

Cortical neurons were prepared from brains of C57/BL6 or *Mast1* KO P0 mice while P7 mice were used for cerebellar neuronal cultures. In short, the brain region of interest was isolated, and the meninges carefully removed. The tissue was treated with 0.25% trypsin solution in a 37°C water bath for 15 mins, followed by three washes in HBSS (20 mM HEPES, 2 mM CaCl₂, 5.4 mM KCl, 1 mM MgCl₂, 1 mM NaPi, 5.6 mM glucose, pH 7.3). The trypsinised tissue was titrated in plating media (DMEM, 10% Horse serum, 200 mM L-glutamin, 100 mM sodium pyruvate), first using a P1000 pipette and then a P200 pipette. The cells were passed through a 70 µm strainer and the resulting cell suspension counted. Neurons plated at ~1 × 10⁵ cells per well in a 24-well plate containing poly-L-lysine coated coverslips. After 3-4 hr the medium was changed to Neurobasal containing B27, L-glutamine and PenStrep supplements. After 4-5 days in culture the coverslips were fixed in 4% PFA and stained with anti-Map2, anti-Tau and anti-Mast1 antibodies.

In vitro transcription and translation of Mast1 and microtubule-binding assay

These experiments were performed as previously described (Keays et al., 2007; Walden and Cowan, 1993). Briefly, the full-length murine Mast1 cDNA was cloned into the pcDNA 3.1+ vector (Invitrogen) driven by the T7 promoter. The different patient mutations screened were introduced by site-directed mutagenesis using the QuikChange Lightning Multi Site-Directed Mutagenesis Kit (Agilent #210518) kit. Plasmids (20 ng/µL final concentration) were used to drive expression in rabbit reticulocyte lysate (TnT T7 Coupled Reticulocyte Lysate System, Promega) containing 35S-methionine (specific activity: 1000 Ci/mMol; Perkin Elmer). Reactions were incubated at 30°C for 90 min. Prior to co-polymerization reactions, the TnT reaction product was cleared by centrifugation at 60,000 g for 10 min at 4°C. MAP rich porcine brain tubulin (Cytoskeleton #ML116) was depolymerized in tubulin buffer (0.1 M PIPES buffer pH 6.9, 1 mM MgCl₂ and 0.5 mM EGTA) by incubation on ice. Co-polymerization reactions were set up by adding the 35S-labeled Mast1 to MAP rich tubulin (1mg/ml), in tubulin buffer containing 1 mM GTP, 2 mM AMP-PNP and 20 µM taxol. To investigate Mast1 binding to microtubules in either the presence or absence of MAPs, the labeled Mast1 reaction was distributed equally between MAP rich and 99% pure porcine brain tubulin (Cytoskeleton #T240). All co-polymerization reactions were incubated at 30°C for 30 min to promote microtubule polymerization and binding of associated proteins. Reaction products were then loaded onto cushions (0.20 mL) containing 1 M sucrose in tubulin buffer, 0.5 mM GTP, 1 mM AMP-PNP and 10 µM taxol and centrifuged at 60,000 g for 15 min at 30°C. All centrifugations were done in a Beckman TL-100.3 rotor. Proteins in the pellet were solubilized in SDS loading dye and separated in a 7% SDS-PAGE. Radioactivity content of the microtubule pellets obtained was determined following an overnight exposure to a high-sensitive film (KODAK BioMax MR film).

QUANTIFICATION AND STATISTICAL ANALYSIS

All statistical analysis was executed using GraphPad Prism software package (v7.0c). Numbers (n) of animals or replica for experiments are indicated in the text and the statistical test used indicated in individual figure legends. Statistical tests used in this study include the Student's t test, one-way ANOVA with Dunnett's or Tukey's multiple comparisons test, and two-way repeated-measures ANOVA with Bonferroni's multiple comparisons test. Samples and animals were not subject to randomization, but were assigned to experimental groups based on their genotype. Shapiro-Wilk or Kolmogorov-Smirnov tests were applied to assess whether assumptions of normality were met, and corrected for multiple comparisons were necessary. A summary of the statistical tests applied for each experiment, the n numbers, and the results obtained are shown in Table S4.

DATA AND SOFTWARE AVAILABILITY

In accordance with ethical frameworks and our commitment to patient confidentiality we have not deposited the primary exome sequencing data generated in this study in a community repository.